Mechanical and Electrical Conductivity Studies of PANI-PVA and PANI-PEO Blends

A.R.Subrahmanyam[a], V.Geetha[a], Atul kumar[b], A.Alakanandana[c], J.Siva Kumar[d]

[a]Department of S&H, MVSR Engineering College, Hyderabad, India

[b]DMRL,Kanchanbagh, [c]Department of S&H, GNIT, Hyderabad, India

[d]Department of Physics, Osmania University, Hyderabad, India

subrahmanyam_ar@yahoo.co.in

***Abstract*-Poly aniline (PANI) separately blended with polyvinyl alcohol (PVA) and Polyethylene oxide (PEO) has been prepared by solution cast method using N-Methyl Pyrrolidone (NMP) as common solvent. The structural changes of PANI-PVA and PANI-PEO films were studied by XRD and FTIR techniques. XRD and FTIR studies confirmed the complex formation in polymer blends. The change in the intensities in the polymer blend and appearance of new peaks in the FTIR spectra revealed the blending of poly aniline with PVA and PEO. The physical properties of these polymer blends were analyzed by tensile testing and scanning electron microscopy (SEM). SEM studies revealed the change in surface morphology of pure PANI with blending. From tensile testing, it was observed that PANI-PVA blend is the most promising composition for several industrial applications. The dc conductivity of these polymer blends has been determined in the temperature range 300K to 373K. The dc conductivity of pure PANI is found to be more than PANI-PVA and PANI-PEO blends. The change in the conductivity of this polymer blending at different temperatures depends on intra - chain and inters - chain mobility and are explained by two phase model.**

Keywords-Poly aniline, Polymer blend, Dc conductivity

I. INTRODUCTION

Conducting polymers have recently become an area of wide-spread interest in organic electronics due to their potential application in energy conversion systems such as photovoltaic cells, solar cells, bio sensors etc [1-3]. In view of this, a great deal of interest has been paid to the transport, mechanical, optical and conducting properties of polymers. Amongst conducting polymers poly aniline (PANI) receives greater attention due to its environmental stability, ease of fabrication and the possibility to blend it with thermo plastics. Poly aniline refers to a class of polymers which in the base (none conducting) form is preferred polymer system for many applications [4-5]. However, two major limitations of conducting poly aniline are an inability to process it by conventional methods and its poor mechanical properties. These limitations can be overcome by preparing conducting poly aniline blends and composites which possess the mechanical properties of the insulating host matrix and the electrical properties of the conducting poly aniline guest. When the host is a polymer, the resulting system is termed a poly aniline blend (or composite), but when the host is a non-polymer material (e.g. metal oxides, silica), it is invariably referred to as a composite. Conducting poly aniline blends are a novel class of materials for which the threshold for the onset of electrical conductivity can be reduced to volume fractions well below that required for classical percolation, which is 16% by volume for a conducting material dispersed in an insulating matrix in three dimensions. Due to a low percolation threshold and a continuous increase in conductivity, j (*f*), for volume fractions (*f*) above the threshold, conducting poly aniline blends can be reproducibly fabricated with controlled levels of electrical conductivity while retaining the desired mechanical properties of the polymer matrix [6]. These blends have potential applications in electromagnetic shielding, electricity dissipation, conducting glues and sensor materials [7-11]. A blend is a mixture of two or more polymers. Blending opens up a root for a combination of different properties. Some recent results indicate that conducting polymer composite materials may have significantly improved electronic and mechanical properties as compared to pure conducting polymer films, making the composite more suitable for microelectronic applications. Already much of the research done in this field, it had been evident that the intrinsic properties of the components of the blends were changed.

II. EXPERIMENTS

Blends of PANI (emeraldine base, Elche mop, India) with PEO (Aldrich), PVA (Loba Chemie) were prepared by solution cast technique using N-Methyl Pyrrolidone (NMP) as a common solvent. Pure PANI was initially taken in NMP solution and stirred for 2 hrs. Then the copolymer such as PEO, PVA was added in equal amount to this mixture and stirred again for nearly 12 hrs. Then this homogeneous mixture was filtered, poured in a glass dish and kept in an oven maintained at 60^0Cto get slowly evaporated. The final product was vacuum dried thoroughly at 10^{-3}Torr. In this manner film of pure PANI, PANI+PEO, PANI+PVA were prepared.

The XRD studies of these samples were carried out with the help of PHILIPS PW 3710 Diffract meter in the range 10^0-80^0. The FTIR spectra of these samples have been recorded with the help of JASCO FTIR-5300 Spectrophotometer in the range 400-4000 cm^{-1} with resolution of 2 cm^{-1}. The mechanical strength of these polymers has been estimated using micro tensile testing machine. The surface morphology of these polymer blends were studied by scanning electron microscopy (SEM) instrument with gold sputtered coated films. The dc conductivity measurements of these polymer blends was measured in the temperature range from 300 – 400 K using two probe method.

III. RESULTS AND DISCUSSIONS

The X-Ray diffraction pattern for pure PANI, PANI+PVA and PANI+PEO films are shown in Figure 1.1 and 1.2. The diffraction pattern of pure PANI and PVA indicates the amorphous nature while that of PEO showed semi crystalline nature. The diffraction pattern of pure PANI has a broad peak around $2\theta = 23.44^0$ which is a characteristic peak of PANI [12]. The characteristic peak of PANI has been shifted slightly

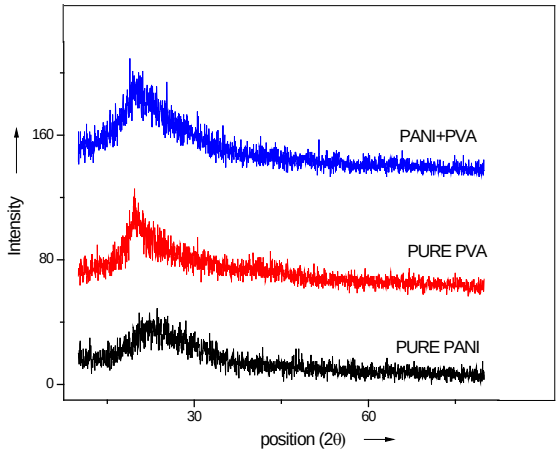

Figure 1.1

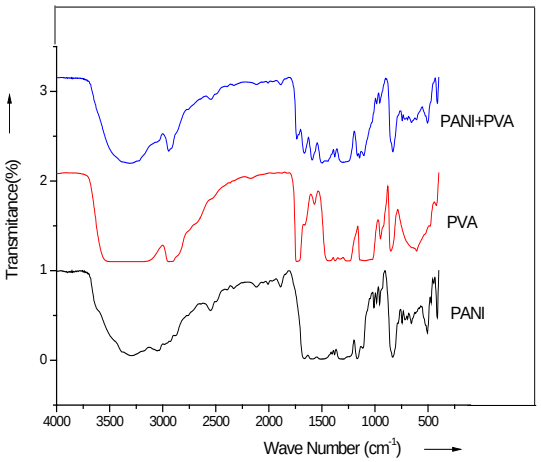

Figure 2.1

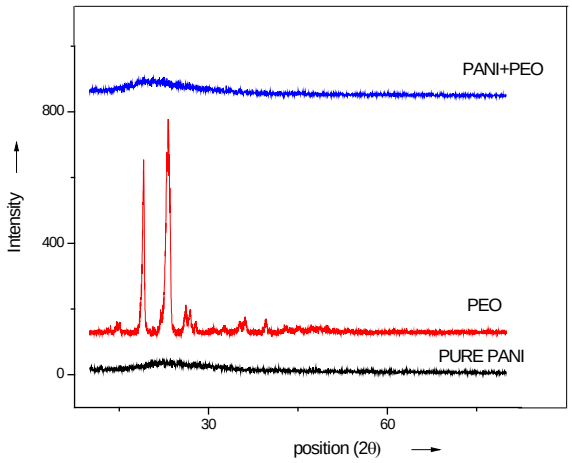

Figure 1.2

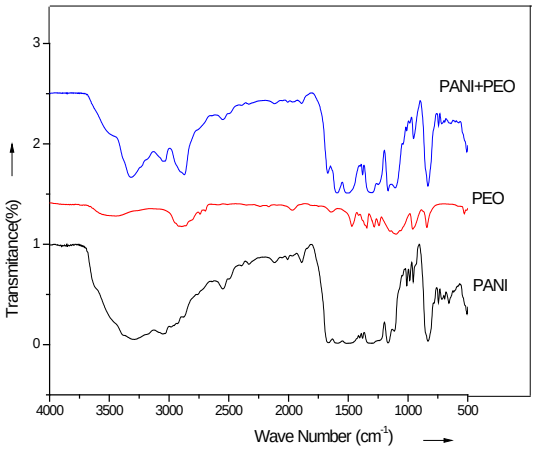

Figure 2.2

TableI OBSERVED CHARACTERISTIC VIBRATIONS FROM FTIR

Characteristic vibration	References	PANI	PVA	PEO	PANI+PVA	PANI+PEO
N-H stretching	3450	3306.64			3318.16	3318
Aromatic C-H stretching	2925	3006.81			2934.19	3037
C-N stretching	1560	1568.99			1610.51	
Aliphatic C-H stretching (PEO)	2897.1			2889.26		2868
C-O stretching (PEO)	1095.2			1076.6		1113.7
O-H stretching (PVA)	3300		3565.5		3356.04	
C-H stretching (PVA)	2930		2921.6		2925.25	

in PANI blends as shown in figures. The XRD pattern of these polymer blends does not show sharp peaks which confirm the amorphous nature of polymer blends. [13-14]

The FTIR spectra of pure PANI and PANI blends are shown in Figure 2.1 and 2.2. From FTIR data it is clear that new peaks corresponding to PVA and PEO are observed in the blended poly aniline. The appearance of new peaks along with changes in existing peaks directly indicates the blend formation. The positions and observed characteristic bands are tabulated in Table 1. The obtained values are in good agreement with theoretical prediction

The surface morphology of PANI and PANI blended with PVA and PEO were studied using SEM technique. The micrographs of the blended films are presented in Figure 3. In the SEM figures it was observed that PANI grains are embedded in the co-polymer matrix.

The mechanical properties in the blended films are compared with pure PANI by using micro tensile testing machine. The stress – strain curves of the polymer blends obtained and the values of Young's modulus are tabulated in the Table 2. The stress-strain data clearly indicates that PANI

+ PVA polymer blend more flexible than pure PANI and PANI + PEO blend.

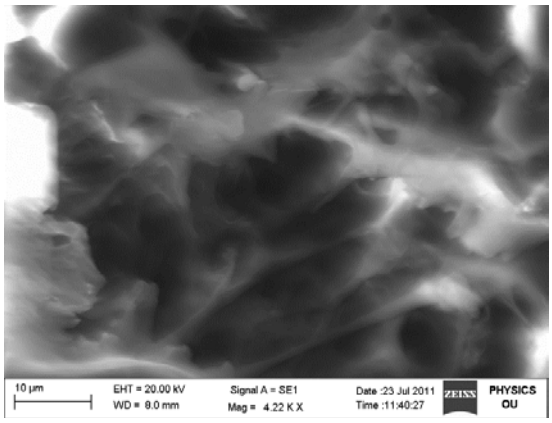

PURE PANI

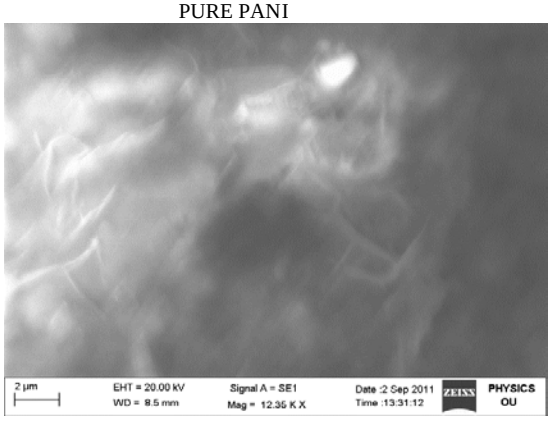

PANI+PVA

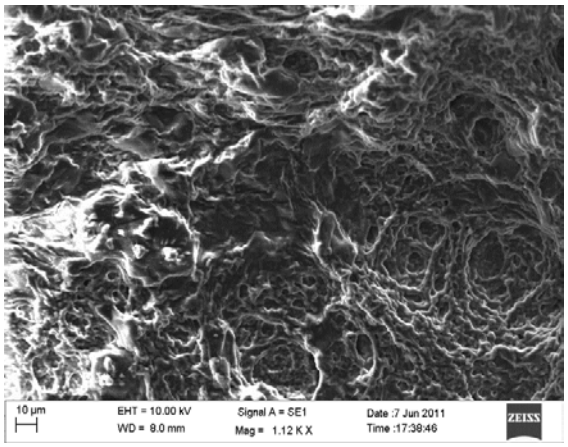

PANI+PEO

Figure3. SEM micrographs of polymer blends

TableII

Polymer	Young's modulus
PANI	0.17
PANI+PVA	0.89
PANI+PEO	3.71

The temperature dependence conductivity of Pure PANI, PANI +PVA and PANI+PEO films is presented in Figure 4. The over-all mobility of charge carriers in conducting polymer blends depends on inter-chain mobility and intra-chain mobility. In PANI-based polymer blends two stages of percolation threshold may be observed, with one corresponding to the well blended phase and the other to the separated phase [15]. The Dc conductivity data suggests that the conductivity of PANI+PEO blend is due to the hopping mechanism between Ether group of PEO and conducting poly aniline. The low conductivity of these polymer blends when compared with pure PANI could be a direct effect of molecular electronic features which improved the degree of crystalline nature but not the conductivity [16]. The conductivity in these blends may be enhanced by doping laterally linked rich donor acceptor groups. Further studies are in progress.

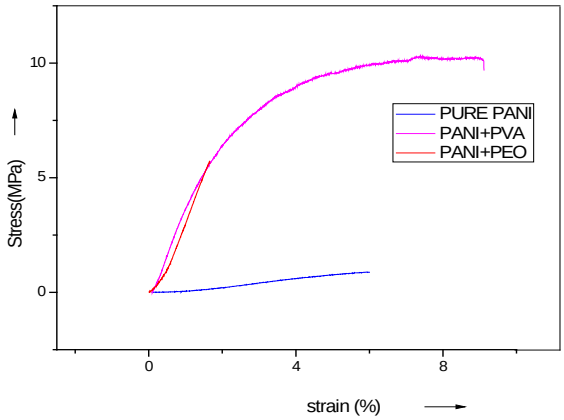

Figure4. Mechanical behavior of polymer blends

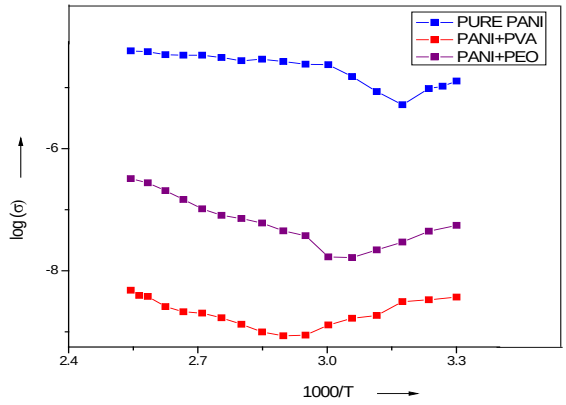

Figure5. Dc conductivity of polymer blends

IV. CONCLUSIONS

In the present work Pure PANI and its blends with PVA, PEO were prepared by solution cast method. The blends were characterized by XRD, FTIR and SEM techniques. It is found that the conductivity of pure PANI is more than PANI blends. The blends were prepared in order to combine the mechanical properties of PVA, PEO with conducting properties of PANI.

ACKNOWLEDGEMENTS

The authors thank the Head and chairman of department of physics, Board of studies in physics, Osmania University for their constant encouragement. Also, the authors thank the coordinator, SAP, department of physics for providing the necessary facilities. One of the authors ARS thanks the Principal, Head, department of S&H, MVSR Engineering College for their constant encouragement. One of the authors

KA thanks the Director, G.Narayanamma Institute of Technology and Science for their consistent encouragement.

REFERENCES

[1] Mac Callum J R, Vincent C A (Eds) (1987) polymer electrolyte rev. Elsevier.Amsterdam

[2] Armand M B (1986) Mater.Sci 16:245

[3] Ratner M A, Shrivar D F (1988) Chem. Rev 88: 109

[4] M.Angelopoulos, J.M. Shraw, R.D.Kaplan and S.Perreault, J.Vac.Sci.Technol. B7 No 6,1519(1989)

[5] A.G.MacDiarmid, J.C.Chiang, A.F.Richter and A.J.Epstein. Synth,Met 18, 285 (1987)

[6] Jayashree Anand, Srinivasan palaniappan, D. N.Satyanarayan , Prog. Polym. Sci., Vol 23, 993–1018, 1998.

[7] Bhattacharya A, De A.Prog, Solid state chem., 24(3): (1996) 141-181

[8] Jonas F, Heywang G., Electrochem Acta 39 (8-9) (1994); 1345-1347

[9] Hanhi K, Lonnberg V, Pyoralak, WO patent. 9706213; (1997)

[10] Koul S, Chandra R, Dhawan S K., Sens Actuator B 75(3) (2001) 151-159

[11] J.P.Yang et.al (1998) Synthetic Metals 93; (1998) 169-173

[12] Huang H and Feng X (1993), Zhul J, Nanotechnol, 19 (2008)

[13] Achari V B reddy, T.J.R. Sharma, A.K, NarasimhaRao V V R, Int.J.of Polymeric Mater 56(2007) 579

[14] Wan M and Li J., J.Polym. Sci. A. (1998) 362799

[15] K Abbas, S.J.Barton, P J S Foot and H.Morgan, Polymers and Polymer Composites 15(2007) 1- 8

[16] N.F.Mott and E A Davis, philos. Mag, vol 7, (1970) 22

Radio-Frequency Power Graded Hydrogenated Amorphous Carbon Films on Diverse Substrates

Yujie Huang[#1], Qi Wang[#2], Mei Wang[#3], Musen Li [#4]

[#]Key Laboratory for Liquid-Solid Structural Evolution and Processing of Materials (Ministry of Education), Shandong University, People's Republic of China

[1]hyjsdu@126.com; [2]wangqi1016@gmail.com

[3]wm8312@gmail.com; [4]msli@sdu.edu.cn

***Abstract*-Diamond-like carbon (DLC) films are increasingly used for optical and biological components. Yet the stability of the film, including adhesion and duration are still to be developed. Hydrogenated DLC films (hydrogenated amorphous carbon, a-C: H) were deposited onto transparent substrates by applying a graded radio-frequency (RF) power by plasma-enhanced chemical vapor deposition (PECVD). The a-C: H film, formed by constant RF power was synthesized for comparison. Raman spectra, X-ray photoelectron spectra (XPS), field emission scanning electron microscopy (FESEM) and atomic force microscopy (AFM) were used to characterize the film structure along with surface morphology and roughness on the diverse substrates. Tribological properties and adhesion were obtained by friction-wear experiment and scratch tests. Light transmittance was determined by UV/Vis spectra. The results have revealed that films deposited on the various substrates had typical diamond-like features and there were obvious residual stress relaxation and better adhesion for the graded a-C: H films.**

Keywords-a-C: H; Microstructure; Residual stress; Adhesion; AFM

I. INTRODUCTION

Diamond-like carbon (DLC) films have many attractive mechanical and optical properties. Researches towards industrial applications of DLC films were widely carried out in the past decades and remarkable successes have been achieved. Protective layers on engineering tools and hard storage discs are the primary uses as a result of its extreme high hardness and wear-resistance [1-2]. DLC films also can be the antireflective coatings for IR optics due to the transparency in the Vis and IR range [3]. Generally, thick films are required to provide protection. However it was reported that DLC films peeled off from the underlying substrates were with thicknesses exceeding 1μm or even 200 nm [4-5]. High residual stress in the DLC films is mostly responsible for this observed poor adhesion. Successive energetic ion bombardment to the growing film surface during the deposition process leads to intrinsic compressive stress in the unbalanced film structure, which is the dominating part of the residual stress [4]. Thus high sp^3 bond content usually accompanies with large intrinsic compressive stress. The tribological property of DLC films are greatly influenced due to the residual stress, with the film continuity and durability being deteriorated. There would be thickness limitation to guarantee enough adhesion of the films coated on substrates. A series of ways were adopted to reduce residual stresses on the films. Addition of interlayers is a common method to reduce such stress. Chehung Wei et al. used two interlayers of chromium and titanium to improve adhesion [6]. Certain elements or metal particles are doped to obtain DLC films of low residual stress, such as Si, N, Ti, Cu and Al [7-11]. Besides, annealing treatment and gradient films are also effective methods [12-14].

Hydrogenated DLC films, i.e. hydrogenated amorphous carbon (a-C: H) are relatively soft and polymeric. In this study, a-C: H films are prepared using plasma enhanced chemical vapor deposition (PECVD) with graded RF power on several transparent substrates which tend to be used in the optical and biological fields, such as glass, indium tin oxide (ITO) coated glass and polyethylene terephthalate (PET) substrates.

II. EXPERIMENTAL

A. Deposition of the a-C: H Films

The a-C: H films were prepared by a self-made PECVD device shown in Fig.1, with a magnetic filed adopted on the cathode plate to control the plasma trace. Prior to deposition, the substrates were cut into 25mm×25mm. The ITO (1.1mm thickness, 10Ω) glass and PET substrates were cleaned in acetone and absolute alcohol each for 15minutes. Silica glass and frosted glass substrates were bathed in alkali solution and acid solution each for 3 hours, with acetone and absolute alcohol cleaning ultrasonically both for 15 minutes succeeded. All the substrates were dried by nitrogen and placed on the anode plate. The distance between the cathode and anode plates was 100 mm. The base pressure in the vacuum chamber was 7.5×10^{-3} Pa. C_4H_{10} and Ar were employed as the reaction gas and the flow rate was 1.5:25. Pre-treatment of Ar^+ bombardment was taken for 15 minutes. During the deposition process, the RF power was stepwise increased from 510 W to finally 720 W for altogether 40 minutes. Therefore, the film composition (sp^3/sp^2 ratio) would be graded through the whole film. The single a-C: H film was deposited on silica glass with constant RF power of 720 W at the same time.

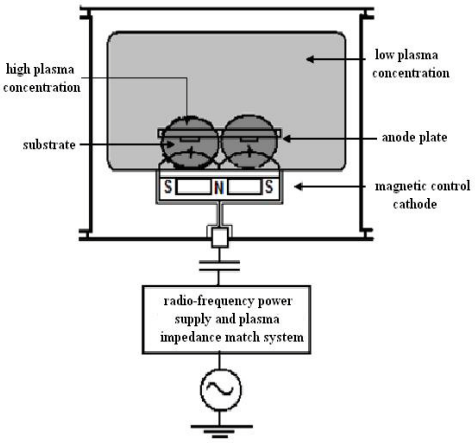

Fig.1. Schematic diagram of radio-frequency magnetron PECVD deposition device

B. Characterization of the a-C: H Films

The type of bonds, relative content and evaluation of residual stress were analyzed by visible Raman spectroscope of LabRAM HR, with the laser excitation at the wavelength of 532.1nm. The film composition was measured by X-ray photoelectron spectroscopy of PHI5300. Surface morphology and roughness were characterized by AFM spectroscopy of Dimension Icon in scanAsyst mode. MS-T3000 friction-wear spectrometer was used to obtain the wear curve and friction coefficient in the ambient environment. The stainless steel ball was used as the counterpart and its rotation speed was 100 rev/min. The load applied was 200 mN. Scratch test was carried out to examine the adhesion strength by WS-2004 scratch tester, with the indenter running speed of 4 mm/min and maximum load of 100N. The morphology of the scratch fragment was seen by field emission scanning electron microscopy of HITACHI SU70. The light transmittance was obtained by ultraviolet–visible (UV–vis) spectrophotometer of TU-1901.

III. RESULTS AND DISCUSSION

A. Bonding Microstructure and Surface Morphology

Bonding structural characteristics of DLC films are generally given by Raman spectroscopy. The typical Raman spectrum of DLC films is a broad band between 1200 cm^{-1} and 1800 cm^{-1} which is centered near 1560 cm^{-1} and can be deconvoluted into D peak and G peak by Gaussian fitting. The D band arises from the breathing vibrations of the six-fold aromatic rings of A_{1g} mode at about 1350 cm^{-1}.The G band is due to the stretching vibration mode of sp^2 sites both in rings and chains at about 1580 cm^{-1}. The Raman signal of sp^2 sites is more than 50 times stronger than that of sp^3 bonds, so Raman spectrum of the film is actually dominated by sp^2 sites without direct sp^3 bonding information. Specific details of sp^3 and sp^2 bonds can be provided by the Gaussian fitting parameters of peak position, intensity ratio of I_D/I_G and FWHM of the two fitting peaks. Usually, various deposition conditions can cause the peak shift. Both bond angle removal and bond length disorder lead to a downward shift of the G peak position [15-17].

Raman spectra of the graded and single a-C: H films on different substrates are shown in Fig. 2. It is observed that the Raman spectra of the A-C: H films have similar shapes of the broad asymmetric peaks. The D peaks at about 1350 cm^{-1} and G peaks at around 1590 cm^{-1} are seen exhibiting typical Raman features of DLC films (Fig. 1b). The Gaussian parameter of I_D/I_G ratio often correlates with the sp^2 and sp^3 bonds content. Lower I_D/I_G ratio with the downward shift of G peak position is corresponded to higher sp^3 bonding fraction [18]. It is indicated from the fitting parameters summarized in Tab. 1 that there is minimum sp^3 content for the graded a-C: H film on PET substrate according to its biggest I_D/I_G ratio, which is probably caused by the organic composition of the substrate beneficial for the stable sp^2 configurations. Nevertheless, the Raman fitting information is easily influenced by slight bonding changes of a-C: H films. Though I_D/I_G of the graded a-C: H film on ITO substrate is smaller than others, its G position shifts upward relative to the single film. A positive correlation exists between FWHM of G peak and sp^3 content [19]. Sp^3 content increases when the G peak is in a lower position with larger FWHM. Consequently, it can be concluded that the single film gets the maximum sp^3 content due to its maximal FWHM of G peak comparing with the graded films on diverse substrates. The reasonable explanation is that constant energetic ions impacted to the film by higher RF power easily bring in residual stress concentration which tends to induce more sp^3 sites than the graded RF power. J. Schwan et al. has proved that FWHM of the G peak was linearly corresponding to the inner stress of DLC films [19]. Decrease of the residual stress would result in a reduction of the FWHM. Therefore, the residual stress can be predicted to decrease by using the graded RF power. Additionally, there is particularly less stress concentration for a-C: H on PET than on other substrates (Tab. 1). FWHM broadening of G peak also reflects the disorder of bond angle and bond length as well as decrease of the sp^2 cluster size [16]. As thus it's suggested that the bonding structure of single a-C: H is more disordered than that of the graded a-C: H films.

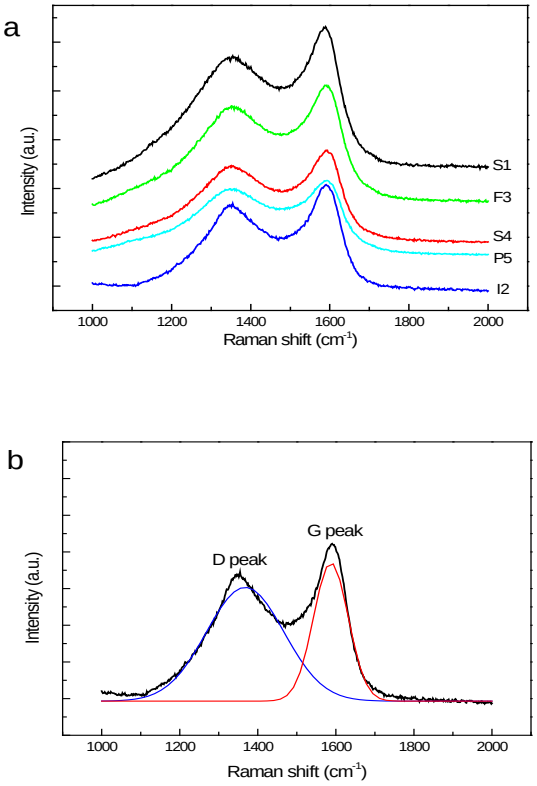

Fig.2. (a) Raman spectra of the a-C: H films on diverse substrates (b) Gaussian fitting peaks of the graded a-C: H on ITO glass substrate

TABLE 1
GAUSSIAN FITTING PARAMETERS OF THE A-C: H FILMS

NO.	Substrate	Power type	D peak position (cm^{-1})	G peak		I_D/I_G
				Position (cm^{-1})	FWHM (cm^{-1})	
S1	SiO2 glass	Single power	1354.69	1589.06	92.55	2.35
I2	ITO glass	Graded power	1354.69	1590.63	89.10	1.84
F3	Frosted glass		1353.13	1592.19	89.78	2.40
S4	SiO2 glass		1351.56	1593.75	87.49	2.58
P5	PET		1348	1593.75	85.29	3.10

The XPS spectrum of the graded a-C: H film on ITO substrate is shown in Fig. 3. Next to the C1s band at 284.58 eV, O1s band at 551.20 eV is observed. (Fig. 3a). The C 1s peak is fitted by three peaks representing C sp^3 at the binding energy of 284.89eV, C sp^2 at 283.31eV, and C=O at 287.69eV (Fig. 3b). Sp^3 bonding fraction is directly measured by the ratio of sp^3 peak area over the whole C 1s peak area [20].

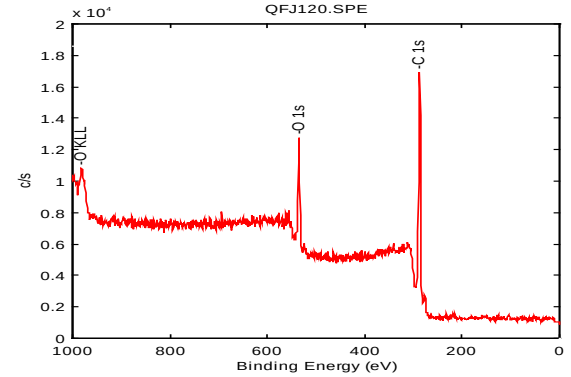

(a)

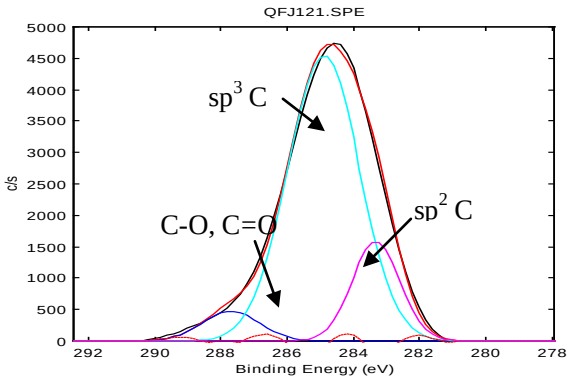

(b)

Fig.3. (a) XPS spectrum of the graded a-C: H on ITO glass substrate and (b) XPS spectrum of the C1s peak

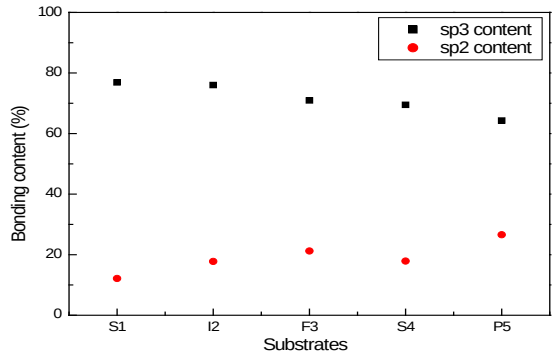

Fig.4. Bonds content of the films obtained by XPS spectra

Fig. 4 shows the bonding fraction of the a-C: H films. As can be seen, surface sp^3 fraction of the graded films is lower than that of the single a-C: H which is up to 76.90%. However, sp^2 fraction is decreased for the graded films. The a-C: H on PET substrate especially exhibits the lowest sp^3 bonding content which corresponds with the Raman analysis. (Fig. 2a).Therefore the graded manner of RF power not only helps forming the structure that sp^3/sp^2 ratio stepwise distributed throughout the film, but also bring in the surface sp^3 fraction reduction, as a result of which the film residual stress can be lowered and the film continuity reinforced. But sp^3 fraction of the graded a-C:H films still keeps in high values so as to provide enough protection once coated on certain biological or optical components.

Fig.5. displays the AFM images of the a-C: H coating on different substrates. It is clearly shown that segregation of the carbon particles happened in partial areas of the single a-C: H, thereby the film continuity and smoothness would be influenced. In contrast, the graded a-C: H films are uniformly distributed on the substrates. The difference is that individual spherical particles compact on silica glass substrate to form the graded a-C: H but it appears in a lamellar structure on ITO glass substrate while flocculently positions on PET substrate. Due to the rough appearance of the frosted glass, the image of the a-C: H on it can't be clearly given.

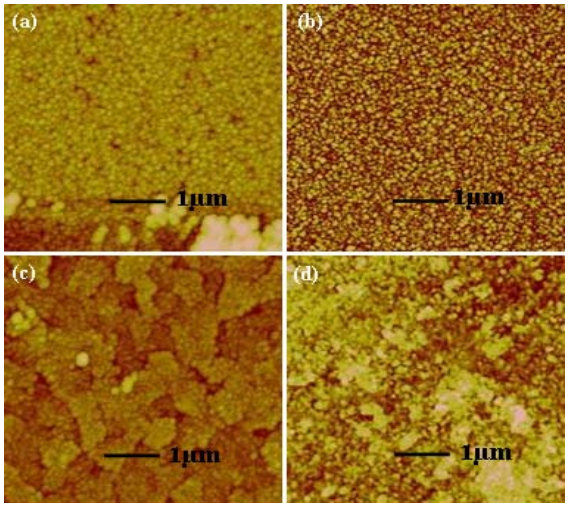

Fig5. AFM images of the films (a) single a-C: H (b) graded a-C: H on SiO2 glass substrate (c) graded a-C: H on ITO glass substrate and (d) graded a-C: H on PET substrate.

The average roughness of the a-C: H is illustrated in Fig.6. Obvious decrease of roughness can be observed for the graded a-C: H films. The a-C: H on the frosted glass substrate owns the lowest roughness primarily attributed to the coarse surface appearance in favour of deposition of the fine carbon particles and prevention against carbon segregation. Consequently it's indicated that the graded RF power would avoid excess carbon molecules from decomposing and deposition so to generate the irregular and aggregated surface, and the morphology of the graded films differed from each other according to the substrates on which they are coated.

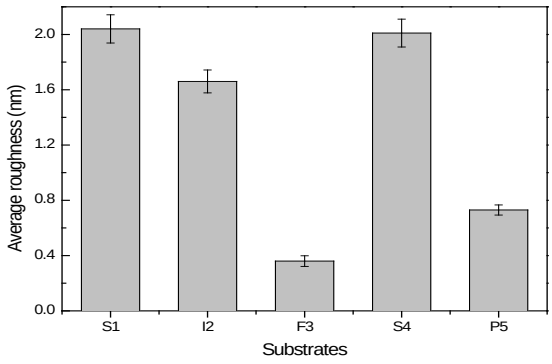

Fig.6. Average roughness of the a-C: H films on different substrates

B. Tribology and Adhesion

Fig.7. presents the wear curves of the a-C: H films. There are obvious increases of the friction coefficient above 0.1 at the beginning for the films and then fall back to 0.1 below as the rotation goes on. In compare with the single a-C: H, wear curves of the graded films work smoothly on the whole. The friction coefficients of graded films coated on silica glass, ITO glass and the frosted glass substrates are approximate when the wear curves operate in the steady state, and the value is particularly in a low level for a-C: H on PET substrate than others. Besides, it's noticed that the wear curve of the single a-C: H tends to rise at the end of the test while it is on the contrary for the graded films.

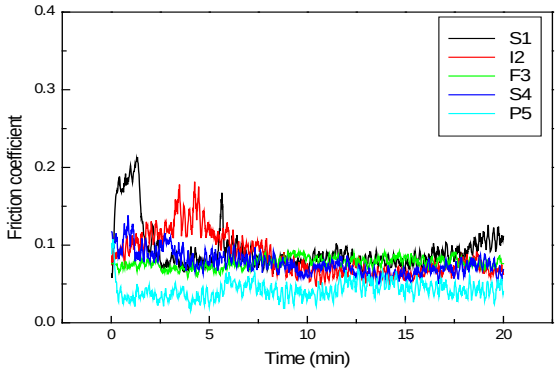

Fig. 7 Variation of friction coefficient against time

With the observation mentioned above, it's merited that the largest average friction coefficient of 0.093 belongs to the single a-C: H, nevertheless the graded a-C: H on PET substrate has the smallest friction coefficient of 0.042 shown in Fig.8. The friction coefficient of graded films on the three types of glass substrates is generally around 0.08. The hydrogen in the a-C: H film can eliminate the free σ-bonds on the film surface which is the main reason for the low friction coefficients [21]. Graphitization of the wear debris lubricates the friction surface that reflects the smooth wear curves. Because the graded structure of a-C: H has lowered the residual stress and promoted the film durability, the friction coefficient of graded a-C: H films is rather low. The surface condition of substrate will also affect the tribological property of a-C: H films.

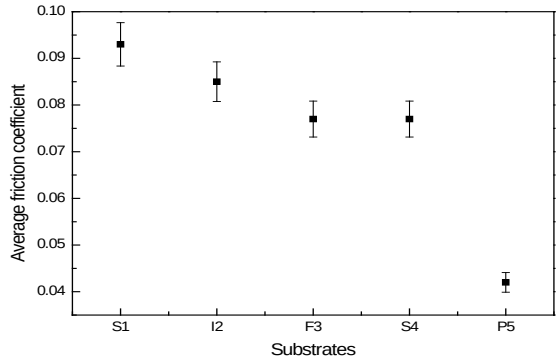

Fig.8 The average friction coefficient versus the substrates

Results of the scratch test are shown in Fig.9. The critical load where the acoustic signal begins to change sharply in the curves with the film adhesive failure can act as a measurement of the film-substrate adhesion strength. The critical load of the single a-C: H is 94.65N. However, it's far beyond the maximum load of 100N for the graded a-C: H on PET and silica glass substrates. The critical load of a-C: H on the frosted glass substrate is still over 100N which will not be affected by the fluctuation of the scratch curve owning to the rough surface of the substrate itself. Only the a-C: H on ITO substrate has the critical load of 94.475N close to that of the single a-C: H. Thus it confirms the improved and more sufficient adherence of the graded a-C: H on the transparent substrates. In addition, the residual stress of the graded a-C: H is indicated to be markedly reduced by comparing the scratch curves.

Fig. 10 is the FESEM image of the graded a-C: H film fragments around the scratch trace on silica substrate. It is obvious that the a-C: H peels off from substrate in the shape of flakes.

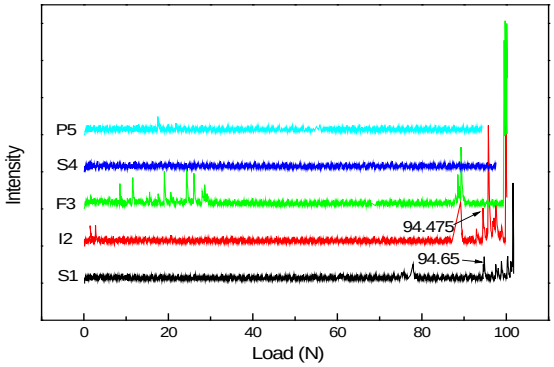

Fig.9 Scratch curves of the a-C: H films.

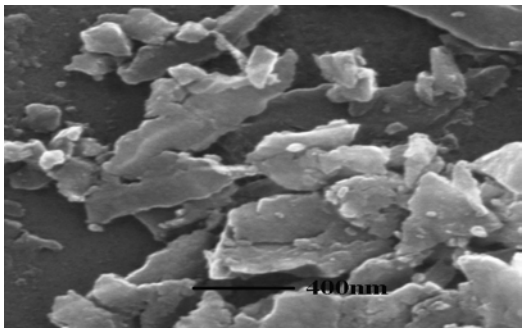

Fig.10 SEM morphology of the a-C: H film fragments

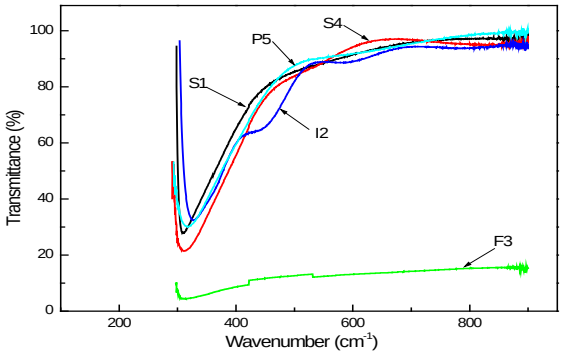

Fig.11 UV/Vis spectra of the a-C: H films.

C. Optical Property

UV/Vis spectra of the a-C: H films are presented in Fig. 11. The single and graded a-C: H films on PET and silica glass substrates have similar light transmittance curves.

There is a stepwise rise of the light transmittance between the wavelength 300 cm^{-1} to 700 cm^{-1} for the a-C: H coated on ITO substrate probably related to multilayer of indium tin oxide film and the a-C: H film. The light transmittance of a-C: H on the frosted glass substrate caused by its irregular surface condition is less than 20%, while it is the highest beyond 700 cm^{-1} for a-C: H on PET substrate. The light transmittance of a-C: H films on silica glass, ITO glass and PET substrates is all greater than 90%, exhibiting excellent transparency of the a-C: H in the visible and near-infrared light region.

IV. CONCLUSIONS

The gradient A-C: H film structure of relatively more sp^2 sites at the film-substrate interface and higher surface sp^3 bond content help ease the severe ion bombardment to the growing film during the deposition process. So the residual stress of the graded a-C: H will be greatly reduced compared with the a-C: H prepared by constant RF power which gets the confirmation from Raman spectra analysis and scratch tests. Moreover, surface quality of the graded a-C: H is improved given by the AFM images. Therefore, the graded a-C: H provides good tribological property of stable wear curve and lower friction coefficient. Film on PET substrate particularly shows favorable adhesion as well as frictional and optical property. In conclusion, the graded a-C: H we synthesized is a proper candidate for the protective coatings on biological and optical substrates.

ACKNOWLEDGMENT

This work is supported by the National Nature Science Foundation of China (Grant No.50972078 and No.51002090) and the Outstanding Young Scientist Research Award Fund of Shandong Province (Grant No.BS2010CL028).

REFERENCES

[1] T. Yamamoto, H. Hyodo, Amorphous carbon overcoat for thin-film disk. Tribology International 36 (2003) 483.

[2] P. Goglia, J.Berkowitz, Diamond-like carbon applications in high density hard disc recording heads. Diamond Relat. Mater. 10 (2001) 271.

[3] Grill, Diamond-like carbon: state of the art. Diamond Relat. Mater. 8 (1999) 428.

[4] E. Mounier, Y. Pauleau, Mechanisms of intrinsic stress generation in amorphous carbon thin films. Diamond Relat. Mater. 6 (1997) 1182.

[5] Q. Hou, J. Gao, Mod. Phys. Lett. B11 (1997) 757.

[6] Wei, J. Yen, Effect of film thickness and interlayer on the adhesion strength of diamond like carbon films on different substrates. Diamond Relat. Mater. 16 (2007) 1325.

[7] P. Papakonstantinou, J. F Zhao, The effects of Si incorporation on the electrochemical and nanomechanical properties of DLC thin films. Diamond Relat. Mater. 11 (2002) 1074.

[8] Anita, T. Butuda, Effect of N doping on properties of diamond-like carbon thin films produced by RF capacitively coupled chemical vapor deposition from different precursors. Diamond Relat. Mater. 13 (2004) 1993.

[9] S. Zhang, X. Lam Bui, Towards high adherent and tough a-C coatings. Thin Solid Films (2005) 138.

[10] J. Jao, S. Han, Bias voltage effect on the structure and property of the (Ti: Cu)-DLC films fabricated by cathodic arc plasma. Diamond Relat. Mater. 20 (2011) 123.

[11] W. Wu, J.Ting, Growth and characteristics of carbon films with nano-sized metal particles. Thin Solid Films 420-421 (2002) 166.

[12] W. Wu, M. Hon, Thermal stability of diamond-like carbon films with added silicon. Surf. Coat. Technol 111 (1999) 134.

[13] A. Ogwu, R. W. Lamberton, Characterisation of thermally annealed diamond like carbon (DLC) and silicon modfied DLC flms by Raman spectroscopy. Physica B 269 (1999) 335.

[14] Donnet, J. Fontaine, Diamond-like carbon-based functionally gradient coatings for space tribology. Surf. Coat. Technol 120-121 (1999) 548.

[15] C. Ferrari, J. Robertson, Interpretation of Raman spectra of disordered and amorphous carbon. Phys. Rev. B 61 (2000) 14095-14107.

[16] C. Ferrari, S. E. Rodil, Interpretation of infrared and Raman spectra of amorphous carbon nitrides. Pysical Review B,2003,67:155306.

[17] S. R. Salis, D. J. Gardiner, Monitoring the quality of diamond films using Raman spectra excited at 514.5 nm and 633 nm. Diamond Relat. Mater. 5 (1996) 589.

[18] J. Robertson, Diamond-like amorphous carbon. Mater. Sci. Eng. R Rep. 37 (2002) 129

[19] J. Schwan, S. Ulrich, Raman spectrascopy on amorphous carbon films. Appl. Phys 1996,80:440.

[20] P. Me´rel, M. Tabbal, Direct evaluation of the sp3 content in diamond-like carbon films by XPS. Applied Surface Science 136 (1998) 105

[21] Erdemir, The role of hydrogen in tribological properties of diamond-like carbon. Surf. Coat. Technol. 146-147 (2001) 292.

Effect of Poly (Toluene Sulphonic Acid) in Enhancing Durability of Poly (Pyrrole)/Poly (N-Methylpyrrole)/GOx Composite Glucose Biosensor

Santosh B. Kadam[#], S. S. Hussaini[+], Kunal Datta[#], Prasanta Ghosh[#], Mahendra D. Shirsat[*#]

[#]Intelligent Materials Research Laboratory, Department of Physics,

Dr. Babasaheb Ambedkar Marathwada University, India

[+]Department of Physics, Milliya Arts, Science and Management Science College, India

[*]mdshirsat_bamu@yahoo.co.in

Abstract-**The effect of poly (tolune sulphonic acid) in enhancing durability of (poly) pyrrole/ (poly) N-methyl pyrrole/ glucose oxidase sensor has been reported in the present investigation. The (poly) pyrrole/ (poly) N-methyl pyrrole composite matrix was synthesized by galvanostatic technique. The poly (toluene sulphonic acid) was added as dopant to enhance susceptibility of the synthesized matrix towards humidity. The polypyrrole – poly (n-methylpyrrole) composite films were subjected to spectral and morphological characterizations. Excellent morphology, suitable for immobilization of glucose–oxidase, was achieved with optimized process parameters. The glucose–oxidase was immobilized on the composite matrix by cross linking via glutaraldehyde. Comparative study was carried out to investigate functionality of the sensor in phosphate and acetate buffer atmosphere. The biosensor exhibited an excellent linear response for a wide range of glucose concentration from 0mM to 10mM in both the buffers. However the sensitivity of the developed biosensor in presence of phosphate buffer (0.41 µA/mM) was found to be higher. The durability of the sensor was found to be excellent (47 days) in presence of poly (toluene sulphonic acid) in phosphate buffer.**

Keywords-Glucose biosensor; Polypyrrole; Poly (N-methyl pyrrole); Composite; Electropolymerization; Poly (Toluene sulphonic acid)

I. INTRODUCTION

Organic Conducting Polymers (OCPs) are well known to be used as enzyme immobilization matrix for development of biosensors [1]–[6]. Extensive study has revealed that a varied spectrum of functionalities can be incorporated in OCP matrix during or post polymerization condition [7]–[10]. However, an efficient immobilization invariably depends on the macro properties of the matrix (vie surface morphology, adhesively etc.) that need to be tuned by optimizing polymerization conditions (viz type of dopant monomer: dopant conc., deposition current etc.) for reliable and reproducible transduction mechanisms [11] – [14].

The estimation of glucose concentration in blood constitutes an important and high- in demand sector in medical diagnostics. The present paradigm of glucose sensing is primarily based on redox properties of Glucose Oxidase (GODx) and several biosensors have been reported utilizing the mechanism [15]-[17]. OCPs are attractive for immobilization of biocomponents, which is fundamentally due to the fact that transduction in OCPs takes place at room temperature which is a prerequisite for proper functioning of biomolecules. Moreover, the conductivity level of OCP films can be controlled to suit the specific requirements of enzymatic activity. However the foremost problem that is encountered by any OPC-based sensors is the degradation of the same under even normal atmospheric condition. The most popular OCPs viz. Polyaniline, Polypyrrole etc. are reported to suffer such degradation [18], [19]. Among various factors, the presence of oxygen and humidity plays the most prominent role in destabilizing the performance of OCP sensors.

In pursuit towards a way out of this problem we have employed a composite Poly (pyrrole) [P (py)]/Poly (N-methyl pyrrole) [P/NMP] matrix for glucose sensing application [20]. In that approach, less susceptibility of P (NMP) and oxygen and humidity was an added advantage over the well-known biocompatibility, high conductivity [21], and ease of synthesis of P (Py).

The present investigation is a continuation of our previous studies. Here we report a glucose sensor with P (Py)/P (NMP) composite matrix synthesized with Ploy (Toluene Sulphonic Acid) (pTS) as a dopant. The choice of dopant was supported by the fact that presence of pTS in OCP atmosphere is reported to cause a reduction in moisture content [22]. Moreover, one of our composite P (Py)/P (NMP) film synthesized with pTS as a dopant exhibit excellent electrical and structural properties are highly suitable for enzyme entrapment.

II. EXPERIMENTAL PART

A. Preparation of P(Py)/ P(NMP)/ pTS Film

Chronopotentiometric technique was employed for the synthesis of P (Py)/P (NMP)/pTS composite film. The electrolyte solution (20ml) consisted of 0.1M Py, 0.1M NMP and 0.1M pTS in double de-ionized water. The monomers Py (98.1%) and NMP (98%) were obtained from Alfa Aesar and Acros Organics respectively. Dopant pTS was procured from Rankem (India). The monomers were double distilled prior synthesis. The synthesis was carried out in a conventional three electrode cell with planar Platinum foil as working and counter electrode and Ag/AgCl as reference electrode. Optimized current density (1mA/cm^2), deposition time (5 min) and pH (3.0) were employed for efficient surface morphology. The synthesis was carried out under ambient conditions. The synthesized films (on platinum substrate) were rinsed with double deionised water to wash out loosely-bounded particles and dried in normal conditions. The synthesis and electrochemical characterization was carried away with CHI 660C electrochemical workstation. The formation of P (Py)/P (NMP) composite was confirmed by FTIR spectral study

using Testscan Shimadzu FTIR- 800 series UV –Visible spectrophotometer in region between 400 and 4000 cm^{-1}. Scanning Electron Micrographs were recorded at different magnifications using JEOL JSM-630, an analytical scanning electron microscope.

B. Immobilization of GOx on P(Py)/ P(NMP)/ pTs Film

The stock solutions of Glucose oxidaxe (GOx) (Aldrich) (1mg/ml) were prepared in 0.1M phosphate buffer and acetate buffers respectively. The solutions were kept under continuous and moderate stirring for 24 h before use. GOx was finally immobilized by cross linking via (0.1%) glutaraldehyde (Loba Chemie, India) on P (Py)/ P (NMP)/ pTS films. A 30 min. incubation time was allotted followed by repeated phosphate and/or acetate buffer wash to ensure that the enzyme is not leached out of the film. Optimized concentrations of GOx and glutaraldehyde were employed for efficient enzyme loading and retention [23].

C. Amperometric Determination of Glucose

The stock solution of D-Glucose was prepared in phosphate (0.1 M) and acetate (0.1M) buffers respectively before 24 h of testing and stored at 4^0C. Amperometric response of the biosensor was studied, for gradually increasing concentrations (0-50M) of glucose, using CHI 660C electrochemical workstation. P (Py)/P (NMP)/pTS electrode was maintained at +700 mV version Ag/Agcl reference electrode in phosphate and acetate buffer solution respectively to yield a stable background current [24].

III. RESULTS AND DISCUSSION

A. Sensing Mechanism

In GOx based glucose sensor, the added glucose solution is oxidised redox action of immobilized GOx in presence of dissolved O_2. The following reaction depicts the phenomenon

The generated H_2O_2 is further oxidized at the polymer layer and results in an anodic current according to the following relation-

$$\text{Glucose} + O_2 \xrightarrow{\text{GOx}} \text{Gluconic acid} + H_2O_2 \quad (1)$$

$$H_2O_2 \xrightarrow{\text{PPY/NMP}} O_2 + 2H^+ + 2e^- \quad (2)$$

The conversion of glucose to gluconic acid results in transfer of two protons and two electrons from the substrate to enzyme [25]. The conducting polymer facilitates the transfer of electrons from redox- cofactor to the sensing electrode.

B. Electrochemical Synthesis of P(Py)/P(NMP)/pTS Composite Film

P (Py)/P (NMP)/pTS composite films were synthesized galvanostatically. Optimized process parameters were employed for synthesis. A low polymerization potential was recorded in chronopotentiogram that ensures higher conductivity and uniform surface morphology. Synthesized composite films had uniform morphology and good adhesivity.

C. FTIR Spectra of P(Py)/P(NMP)/pTS Composite Film

The Principal absorption band observed in the FTIR spectrum of the P (Py)/P (NMP)/pTS composite film (Figure not included). The broad peak at 3695 cm^{-1} corresponds to N-H stretching. The absorption band observed at 2779 cm^{-1} is due to C-H vibrations, and the C = O stretching is observed at 1741 cm^{-1}. The band observed at 1452 cm^{-1} is due to C=C stretching. The peak at 2962 cm^{-1} is attributed to the CH_3 stretching. The sharp absorption band observed at 1259 cm^{-1} is due to the ring stretch of n-methyl pyrrole. The FTIR spectral result confirms the formation of poly pyrrole P(Py) and poly n-methyl pyrrole P(NMP).

D. SEM Study of P(Py)/P(NMP)/pTS Film

The SEM image (Fig.1) for pristine P (Py)/P (NMP)/pTS composite film reveals uniform and granular surface morphology. Such morphology is highly suitable for entrapment of enzyme thus rendering higher stability to the biosensor [26].

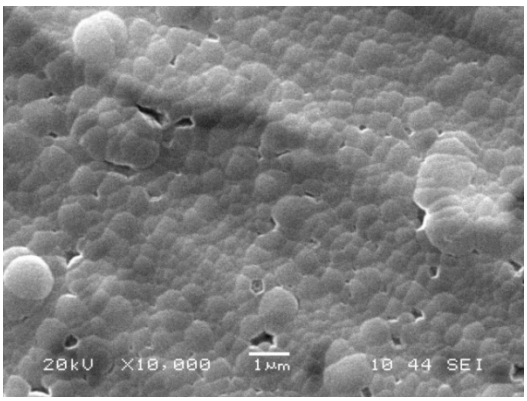

Fig. 1 SEM image of P(Py)/P(NMP)/pTS composite film with optimized process parameters

E. Sensing Response of P(Py)/P(NMP)/pTS/GOx Electrode

The sensitivity of the glucose biosensor is dependent of the GOx entrapped in the electrodeposited polypyrrole film. As it is described earlier, the response of biosensor is proportional to the concentration of H_2O_2 catalytically produced by the GOx on the anode. Thus, the sensing current can determine the relative activity of immobilized GOx.

The P (Py)/P (NMP)/pTS/GOx biosensor responded well in both acetate and phosphate buffer. However, better transduction was recorded for phosphate buffer. The amperometric responses (with electrodes kept at +700mV versus Ag/AgCl reference electrode) of the sensing electrodes in presence of phosphate and acetate buffer are shown in Fig. 2 and Fig. 3 respectively.

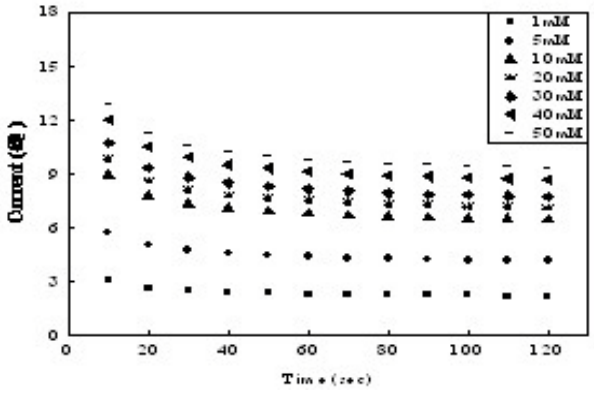

Fig. 2 Current-time relationship(sensing response) of P(Py)/P(NMP)/pTS/GOx electrode in 0.1M phosphate buffer (pH7.4) for different glucose concentrations of 0-50mM: a) 0mM ; b) 1mM ; c) 2mM ; d) 3mM ; e) 4mM ; f) 5mM ; g) 6mM ; h) 7mM ; i) 8mM ; j) 9mM ; k) 10mM ; l) 20mM ; m) 30mM; n) 40mM ; o) 50mM .

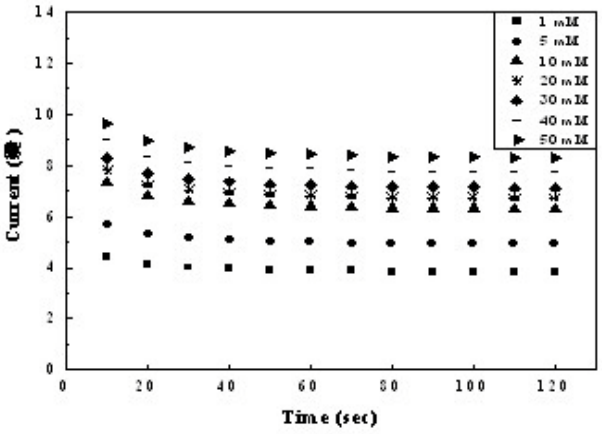

Fig. 3 Current-time relationship(sensing response) of P(Py)/P(NMP)/pTS/GOx electrode in 0.1M acetate buffer (pH7.4) for different glucose concentrations of 0-50mM: a) 0mM ; b) 1mM ; c) 2mM ; d) 3mM ; e) 4mM ; f) 5mM ; g) 6mM ; h) 7mM ; i) 8mM ; j) 9mM ; k) 10mM ; l) 20mM ; m) 30mM; n) 40mM ; o) 50mM .

The response current was found to reach a steady state easily. The relationship between response current and glucose concentration (0-10mM) in 0.1M phosphate buffer (pH 7.4) is shown in Fig.4 (the linear regression equation is $y = 0.499x + 1.548$ and the linear regression coefficient is $R^2 = 0.983$). The inset indicates a linear response from 0mM to 50mM of glucose concentration (The linear regression equation is $y = 0.141x + 3.314$and the linear regression coefficient is $R^2 = 0.797$).

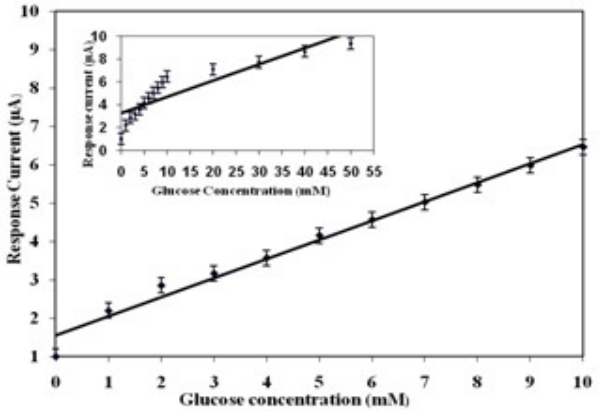

Fig. 4 The relationship between response current and glucose concentration for P(Py)/P(NMP)/pTS/GOx electrode in 0.1M phosphate buffer (pH7.4). The inset indicates the response from 10mM to 50mM.

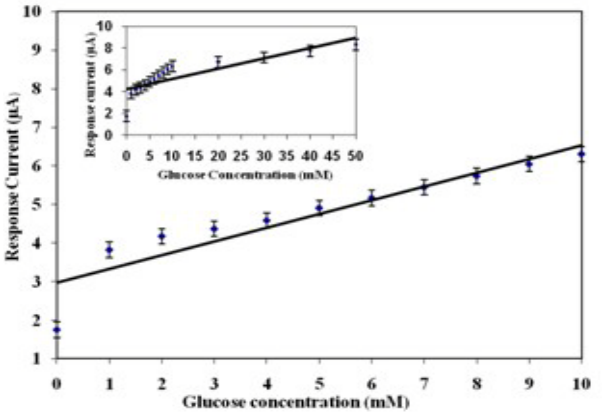

Fig. 5 The relationship between response current and glucose concentration for P(Py)/P(NMP)/pTS/GOx electrode in 0.1M acetate buffer (pH7.4). The inset indicates the response from 10mM to 50mM.

Similarly the linear relationship between response current and glucose concentration (0-10M) in 0.1M acetate buffer (pH 7.4) is shown in Fig. 5 (the linear regression equation is $y = 0.445x+2.954$ and the linear regression coefficient is $R^2 = 0.911$). The inset indicates a linear response from 0mM to 50mM of glucose concentration (The linear regression equation is $y = 0.119x + 4.557$ and the linear regression coefficient is $R^2 = 0.750$).

In both cases, increase in current and glucose concentration have been observed within a range of 0 mM to 50 mM concentration. Steady state response was achieved within ca. 10 s. for each spike of glucose. During successive addition of 1mM of glucose, the increase in response was well defined. The sensitivity of the biosensor in acetate and phosphate buffer is found to be 0.22 µA/mM and 0.41 µA/mM respectively. The detection is sufficient for medical diagnostics purpose since the normal clinical range for glucose in blood is between 3.5 to 6.1 mM whereas abnormal glucose levels can reach as high as 20 mM [25].

F. Stability and Lifetime of the P (Py)/P (NMP)/pTS/GOx Electrode

The long term stability of the P(Py)/P(NMP)/pTS/GOx sensor electrode, in both acetate and phosphate buffer, was tested for 50 days. A steep decrease in current response at initial phase was observed in both cases. The decrease was more pronounced in acetate buffer. At later phases, the responses used to stabilize. A commendable stability of the sensor electrode of 47 days was recorded for Phosphate buffer where as for acetate the stability was about 32 days. The lifetime of the sensor was better than our earlier reported P (Py)/P (NMP)/$NaNO_3$/GOx sensor, an advantage purely attributed to the presence of pTS as dopant. The stability characteristics are given in Fig 6.

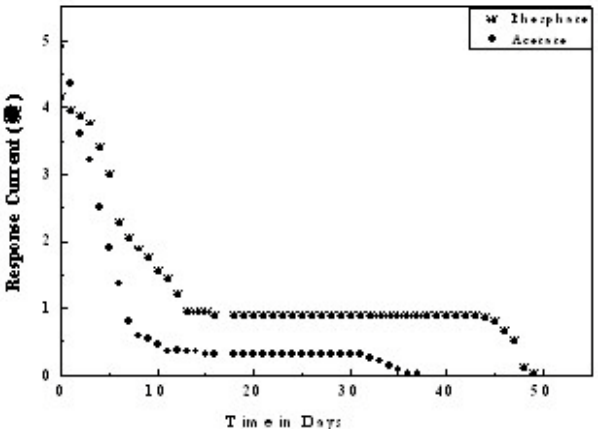

Fig.6 The stability of synthesized P(Py)/P(NMP)/pTS /GOx electrode in phosphate and acetate buffer (7.4 pH) for 5 mM of glucose concentration

IV. CONCLUSIONS

A P (Py)/P (NMP)/pTS composite film has been successfully synthesized by electrochemical technique. The process parameters were suitably optimized to support enzymatic activities for biosensing applications. Glucose Oxidase was immobilized by cross linking (via glutaraldehyde) on the composite matrix for fabrication of a glucose sensor electrode. The sensor exhibited an excellent linearity and fast sensing response to glucose concentration of 0-50mM which is a highly dynamic range suitable for medical diagnostics. A comparative study showed that the sensor operates better in phosphate buffer atmosphere than in acetate buffer. The

composite structure of P (py)/P (NMP) with pTS as a dopant showed an excellent durability of the sensor.

ACKNOWLEDGEMENTS

The authors are grateful to CSIR, INDIA and UGC, INDIA for financial assistance. K. Datta is thankful to CSIR, INDIA for providing a research fellowship. P. Ghosh is thankful to UGC, IUAC INDIA for providing a research fellowship.

REFERENCES

[1] F Palmisano, P.G. Zambonin, D. Centonze, and J. Fresenius, "Amperometric biosensors based on electro synthesised polymeric films," J. Anal Chem., vol. 366, pp.586-601, 2000.

[2] D.J. Shirale, V.K. Gade, P.D. Gaikwad, H.J. Kharat, K.P. Kakde, P.A. Savale, S.S. Hussaini, N.R. Dhumane, and M.D. Shirsat, "Synthesis of P (NMP) film for glucose oxidase electrode," Trans. SAEST., vol.40, pp. 128 -133, 2005.

[3] K.C. Schuhmann. J. Huber, and H. Wohlschlager,"Conducting Polymer-Based Amperometric Enzyme Electrodes. Towards the Development of Miniaturized Reagentless Biosensors," Synthetic Metals., vol.61, pp.31–35, 1993.

[4] J.C. Vidal, J. Espuelas, E. Garcia-Ruiz, and J-R Castillo, "Amperometric cholesterol biosensors based on the electropolymerization of pyrrole and the electrocatalytic effect of Prussian -Blue layers helped with self-assembled monolayers," GEAS, Talanta.,vol. 64,pp. 655 -664,2004.

[5] P.D. Gaikwad, D.J. Shirale, V.K. Gade, P.A. Savale, H.J. Kharat, K.P. Kakde, S.S. Hussaini, N.R. Dhumane, and M.D. Shirsat, "Synthesis of H2SO4 doped polyaniline film by potentiometric method," Bulletin of Material Sci., vol.29, pp.169 – 172, 2006.

[6] S.B. Adeloju and A.N. Moline,"Fabrication of ultra-thin polypyrrole-glucose oxidase film from supporting electrolyte-free monomer solution for potentiometric biosensing of glucose," Biosensors & bioelectronics., vol.16(3),pp.133 – 139,2001.

[7] M.A. Rahman, D. S. Park and Y.B. Shim,"Functionalized conducting polymer as an enzyme-immobilizing substrate: an amperometric glutamate microbiosensor for in vivo measurements," Biosensors Bioelectronics., vol. 19, pp.1565 – 1571,2004.

[8] M.A.Rahman, N-H. Kwon, M–S. Won, E.S. Choe and Y-B. Shim, "Functionalized conducting polymer as an enzyme-immobilizing substrate: an amperometric glutamate microbiosensor for in vivo measurements," Anal. Chem., vol.77, pp. 4854 – 4860, 2005.

[9] A. E. Boyukbayram, S. Kiralp, L.Toppare, and Y. Yagsi,"Preparation of Sensitive Biosensors by Immobilization of Polyphenol oxidase in Conducting Copolymers and Their Application for Determination of Phenolic Compounds in Red Wine", Bioelectrochemistry., vol. 69, pp.164-171,(2006.

[10] A. Chaubey, K.K. Pande, V.S.Singh, and B.D.Malhotra,"co-immobilization of lactate oxidase and lactate dehydrogenase on conducting polyaniline films," Anal. Chem. Acta., vol.407, pp.97-103, 2000.

[11] J. Shirale, V. K. Gade, P. D. Gaikwad, H. J. Kharat, K. P. Kakde, P. A. Savale, S. S. Hussaini, N. R. Dhumane, and M. D. Shirsat, "The influence of electrochemical process parameters on the conductivity of poly(N- methylpyrrole) films by galvanostatic method," Materials Letters.,vol.60, pp. 1407-1411,2006.

[12] K. Gade, D. J. Shirale, P. D. Gaikwad, K.P. Kakde, P. A. Savale, H. J. Kharat, and M. D. Shirsat,"Synthesis and characterization of Ppy-PVS, Ppy-pTS and Ppy-DBS composite films," Int. J. Polym. Mater.,vol.56,pp. 107 – 114, 2007.

[13] W. Su, and J. O. Iroh,"Electrodeposition of poly (n-methylpyrrole) coatings on steel from aqueous medium," J. Appl. Polym. Sci., vol.71, pp. 1293 – 1302, 1999.

[14] A.C. Partridge, C.B. Milestone, C.O. Too and G.G. Wallace, "Polypyrrole based cation transport membranes," J. Membrane Sci., vol.152, pp. 61 – 70, 1999.

[15] D. Olea, P. Moreau, and C. Faure, "Polypyrrole–glucose oxidase biosensor Effect of enzyme encapsulation in multilamellar vesicles on film growth and morphology," J. Electroanalytical Chem., vol. 605, pp. 125 – 135, 2007.

[16] J. Li and X. Lin, "Glucose biosensor based on immobilization of glucose oxidase in poly(o-aminophenol) film on polypyrrole-Pt nanocomposite modified glassy carbon electrode", Biosensors and Bioelectronics., vol.22, pp. 2898 – 2905 , 2007.

[17] A. Rahman, P. Md. Kumar, D. Park, and Y. Shim,"Electrochemical Sensors Based on Organic Conjugated Polymers," Sensors., vol.8,pp. 118 – 141, 2008.

[18] R. Ansari, M. B. Keivani, Polyaniline conducting electroactive polymers, Thermal and Environmental stability studies," E-Journal of Chemistry., vol.3, pp. 202 – 217, 2006.

[19] K. Naoi, T. Hirabayashi, I. Tsubota, and T. Osaka,"Application of Pyrrole/N-Methylpyrrole Composite Polymer to Cathode Active Material of Lithium Secondary Battery," Bulletin of the Chemical Society of Japan., vol.60, pp. 1213 – 1217, 1987.

[20] S. B. Kadam, K. Datta, P. Ghosh and M. D. Shirsat, "Poly(Pyrrole)-Poly(N-Methylpyrrole) Composite Matrix for Amperometric Biosensor Design", Int. J. Polym. Mater., vol 60, pp. 233-243, 2010.

[21] V.K. Gade, D.J. Shirale, P.D. Gaikwad, P. A. Savale, K. P. Kakde, H.J. Kharat, and M. D. Shirsat," Synthesis and characterization of Ppy-PVS, Ppy-pTS and Ppy-DBS composite films," Int. J. Polym. Mater. vol.56, pp. 107 – 114, 2007.

[22] A. Kaynak, L. Wang, C. Hurren, and X. Wang,"Characterization of Conductive Polypyrrole Coated Wool Yarns," Fibers and Polymers., vol. 3(1), pp. 24 – 30, (2002).

[23] D.J. Shirale, V.K. Gade, P.D. Gaikwad, P. A. Savale, K. P. Kakde, H.J. Kharat, and M. D. Shirsat,"Glucose oxidase immobilized on galvanostatically synthesized Poly (N–methylpyrrole)/PolyVinyl Sulfonate film for determination of glucose," Int. J. Polym. Anal. Charac., vol.11, pp. 369 – 382, 2006.

[24] M. U. Yuh, and C. C. Tse, "Fabrication of glucose oxidase/polypyrrole biosensor by galvanostatic method in various pH aqueous solutions", Biosens. Bioelectron., vol. 19, pp. 141-147, 2003.

[25] L. B. Wingard, C. C. Liu, S. K. Wolfson, S. J. Yao, and A. L. Drash, "Potentiometric measurement of glucose concentration with an immobilized glucose oxidase /catalase electrode," Diabetes Care., vol.5,pp. 199 – 202, 1982.

[26] P. A. Savale, M. D. Shirsat, "Synthesis of poly (o-anisidine) / H2SO4 film for the development of glucose biosensor," Appl Biochem Biotechnol.,vol.159,pp.299–309,2009

Micro-Structural Characterization of Cast Mg-TiC MMC's

A. Munitz[#1], I. Jo[*2], J. Nuechterlein[*2], W. Garrett[*2], J.J. Moore[*2], M.J. Kaufman[*2]

#1Nuclear Research Center-Negev,P.O.Box 9001, Beer-Sheva, 841900, ISRAEL

[2*] Department of Metallurgical and Materials Engineering,Colorado School of Mines, Golden, Colorado, USA

Abraham Munitz <unitza@yahoo.com>,Ilguk Jo <ijo@mymail.mines.edu>

Jacob Nuechterlein jnuechte@mines.edu,William Garrett wgarrett@mines.edu

John J Moore jjmoore@mines.edu,Michael J Kaufman <mkaufman@mines.edu>

***Abstract*-Mg-based MMCs containing 10, 20 and 30 vol. % TiC were produced by stirring cold pressed pellets containing micron-size TiC (80 vol. %) and Mg (20 vol. %) powders into molten Mg-9 wt.% Al and casting to produce small billets. These composites were characterized in the as-cast condition and after solution treating and aging using SEM/EDS. Micro-hardness measurements were used to correlate with the microstructures. The as-cast composites consist of Mg-Al dendrites and interdendritic regions are comprised of TiC particles as well as $Mg_{17}Al_{12}$, Mg and Al oxides, and porosity. Isolated TiC agglomerates resulting from incomplete "disintegration" of the TiC pellets were also observed. The oxides and porosity were best near the top of the billets. A solution heat treatment was used to homogenize the matrix and decrease the $Mg_{17}Al_{12}$ and oxides without noticeably affecting the TiC. Aging at 210°C caused micro-structural and hardness changes similar to those for AZ-91 alloys.**

Keywords-Metal Matrix Composites (MMCs); Mg-Al Alloys; TiC; Mechanical Properties; Microstructure

I. INTRODUCTION

There is a growing demand in the automotive industry for reducing vehicle weight to increase efficiency and reduce fuel consumption for lower emission levels. This goal can be achieved by replacing various automotive components (e.g., hoods, doors and bodies) with components made from lightweight metals, like Mg or Al alloys, or using higher strength alloys in thinner cross sections. For the former, the most applicable alloys are those based on Mg-Al, such as AZ91, because of their excellent castability, corrosion resistance, and strength at room temperature [1]-[3]. It is well-known that the strength of the Mg-Al alloys is improved as the Al content increases [4]. Nevertheless, the ductility decreases significantly with increased Al content, which limits the applications of these alloys to less than 9 wt% Al. However, compared to other structural metals, magnesium alloys have a relatively low absolute strength, especially at elevated temperatures, as their applications are usually limited to temperatures of up to 120°C. Further improvements in their high-temperature properties should greatly expand their industrial application [5]. These demands have led to extensive R&D efforts to develop magnesium matrix composites and cost-effective fabrication technologies. For instance, the magnesium matrix composite unidirectionally reinforced by continuous carbon fibbers can readily show a bending strength of 1000 MPa with a density as low as 1.8 g/cm^3 [6]-[7]. The superior mechanical properties can be retained at elevated temperatures of up to 350–400°C [8]-[9]. Another advantage for adding ceramic particles into the Mg alloys is the grain refinement where the particle size affects the matrix grain size and the mechanical properties. For example, Lu et al. [10] showed that a reduction in the SiC size from 50 μm to 10 μm resulted in a grain size change from 43 μm to 23 μm. In general, the use of thermally stable ceramic reinforcements to create Mg based metal matrix composites (MMC) facilitates the retention of enhanced mechanical properties at elevated temperatures [11]. The desirable characteristics of MMCs include enhancements in stiffness, strength, creep resistance, and wear resistance [5]; however, MMCs normally exhibit lower ductility and toughness than the unreinforced matrix [11]. Cao et al. [12], [13] has reported that nanocompositing can actually lead to an increase in the ductility of as-cast magnesium-based metal matrix nanocomposites (MMNCs).

In addition, some Mg alloys such as WE43 are being considered as attractive lightweight materials to manufacture ultra lightweight armoured ground vehicles [14]. The addition of ceramic particles might improve the capability of WE43 for armour applications.

The purpose of this study was to investigate TiC-reinforced Mg alloys using simple casting approaches (e.g. low pressure die casting). The volume fraction and size of the TiC were varied in an effort to characterize its effects on both microstructure and properties

II. EXPERIMENTAL

Pure Mg (99.9%), commercial TiC powder (99.7% purity with grain size of 1~5 μm) and commercial Al powder (99.5 % with average grain size of ~44μm) were used to prepare the Mg-9 wt% Al with 10 to 30 vol.% TiC. The billet dimensions were either 45 or 60 mm diameter and 90 mm height. The amounts of Mg, TiC and the Al were calculated to produce TiC from 10 to 30 vol.%. The TiC and Al powders were weighed according to the desired composition and were mixed using an acoustic vibratory mixer and then they were uniaxially pressed into 12.5 mm diameter cylindrical pellets. The average green density of the pellets was approximately 60% of the theoretical density. The Mg was inserted into boron nitride coated graphite crucible, which was inserted into an iron crucible, which, in turn, was placed in the middle of a 140 kg induction furnace containing an alumina crucible. A protective argon "blanket" was used to cover the melt throughout the entire process to minimize oxidation and the alloy was heated to ~750°C. The molten magnesium was held at 750°C and the desired volume percent of the reinforcement was introduced by submerging the cold pressed pellets into the melt. After their insertion, the "melt" was mechanically stirred for ~5 min using a steel rod to facilitate the

incorporation and uniform distribution of the TiC reinforcement into the melt. During stirring, the temperature was maintained between 750 and 800°C. After stirring, the stirrer was removed and the graphite crucible was extracted and then quenched into water.

The billets containing 10, 20, and 30 vol. % TiC were machined to the desired dimensions and then coated with a commercial 2-part (epoxy / TiB_2 powder) to produce protective coating during the reheating of the billets to above the liquid's temperature of the Mg matrix before placing them into the shot sleeve of an HPDC machine at V-forge die-casting company where they were die cast into either wedge samples or automotive belt tensioning brackets. After casting, the composite materials were heat treated using Mg-AZ91 specifications, i.e. solution heat treated at 413±6°C for 16-24 h, water quenched and then aged at 215±5°C for 5-6 h.

After solidification, the samples were cross-sectioned and prepared using standard metallographic procedures. First, the specimens were abraded on SiC paper to 600 grits and then polished to 1 μm using a diamond paste. After mechanical polishing, the specimens were submerged in a chemical polishing solution and comprised of 100 cc ethanol, 4 cc HNO_3, and 6 cc HCl at room temperature for 5 to 10 sec. Micro-structural examination was performed with scanning electron microscopes (SEM) equipped with energy dispersive spectroscopy (EDS) capabilities. The raw intensity data were corrected with a ZAF computer program [15]. The specimens used for micro-structural examination were also used for Vickers microhardness tests with 1 kg load for 10 s.

For the compression tests, samples with rectangular cross sections were cut with dimensions of 4x4x7 mm. The samples were then compression tested using a crosshead velocity of 1 mm/min.

III. RESULTS AND DISCUSSION

A. Microstructure Examination

A series of backscattered electron images (BEI) illustrating the characteristic microstructure of Mg-9wt.% Al. 10 vol.% TiC are shown in Fig. 1. The microstructure consisted of dark Mg-Al cells matrix (point 4 in Fig. 1b) surrounded by a brighter, higher Z phase (Fig. 1a). First those who need to be solidified are the Mg dendrites which contained up to 9 wt.% Al. The centre of the dendrites is lower in Al and the Al concentration increases towards the interdenritic regions. As solidification proceeds, the TiC particles as well as Al and oxygen are rejected into the interdendritic regions, which solidify last. At higher magnifications, these cells reveal two types of interdendritic microstructures, namely, interdentritic regions which contain a large portion of TiC (Fig. 1a) and those that contain a large portion of $Mg_{17}Al_{12}$ and small amount of TiC (Figs. 1b and 1d). As can be seen in Fig. 1d, the TiC is sometimes embedded in an $Mg_{17}Al_{12}$ phase which is surrounded by an Al- rich layer (about 2 to 3 wt % Al higher than the matrix). EDS analysis indicated the presence of large quantities of oxygen in these regions.

In addition, large areas like point 1 in Fig. 1 can also be seen. At higher magnification (Fig. 1e), this area is observed to consist solely of TiC particles embedded in the Mg matrix with almost no oxides. This is attributed to unintegrated pieces of the TiC pellets which, in spite of the vigorous stirring, did not disperse into the matrix. In contrast, the interdendritic region in Fig. 1f contains a lower density of TiC particles intermixed with $Mg_{17}Al_{12}$ and oxides (Fig. 1f) as well as Mg containing 2 to 3% higher Al than the surrounding matrix (Fig. 1d). Higher magnification of the TiC did not reveal an interaction layer between the TiC and the Mg interface. On the other hand, there were large areas containing interdendritic regions that were composed solely of $Mg_{17}Al_{12}$ as seen in Fig. 1b.

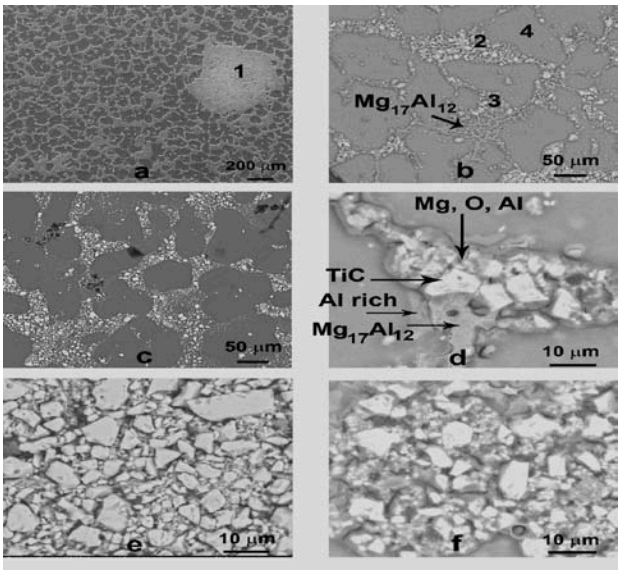

Fig. 1 BEIs illustrating the microstructure of Mg-9wt.%Al + 10 vol.% TiC. (a) overall view; higher magnification of interdendritic regions rich in oxides (b) and TiC (c); (d) higher magnification of the region marked 3 in (b); (e) higher magnification of the region marked 1 in (a); (f) higher magnification of the region marked 2 in (b)

Increasing the TiC in the melt from 10 to 20 vol.% resulted in larger cross-sections of the interdendritic regions and less well developed Mg dendrites (Fig. 2a-b). At 30 vol.% TiC, essentially no dendrite cores were observed (Fig. 2c) although the structure appeared to contain significantly more than 30 vol.% TiC. This has been shown to be an artefact of mechanical polishing [16]. Again, large unintegrated pieces of TiC were also observed in the 30 vol.% TiC material (Fig. 2c).

The effect of solution treatment and aging on the microstructure of the 10 vol.% TiC composite are shown in Fig. 3. Macroscopically, the structure of the Mg dendrites and interdendritic regions could be seen after solution heat treatment. However, microscopic changes associated with aging were too fine to be observed in the SEM images. As expected, the amount of the $Mg_{17}Al_{12}$ phase was reduced although some still existed after the heat treatment. In addition, it appeared that the amount of oxides in the interdendritic regions was reduced by the heat treatment although no attempt was made to quantify this effect. It should be mentioned that, while the majority of the microstructure of the cast billets is similar to that in Figures 1 and 2, there are regions, especially in the upper part of the cast billet near the outer surface, that contain large oxides (the dark phases in Fig. 4). EDS analysis indicated that these oxides contain large O contents as well as a significant amount of sulphur that apparently originated from the TiC powders. The density of the dark particles increased towards the top outer surface. Another type of oxide was found in the interdendritic regions (Figures 1d and 3a-3b). As will be shown below, the oxides reduce the mechanical properties and the workability of the material.

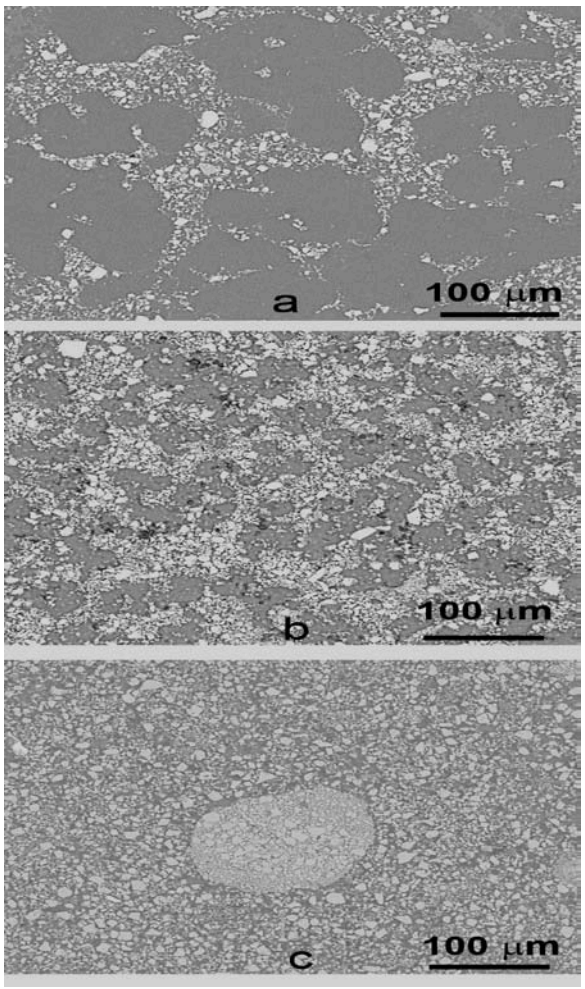

Fig. 2 BEIs illustrating the microstructure of Al-9 wt.% Al as a function of vol.% TiC in the alloy. (a) 10 vol.% (b) 20 vol.% (c) 30 vol.%.

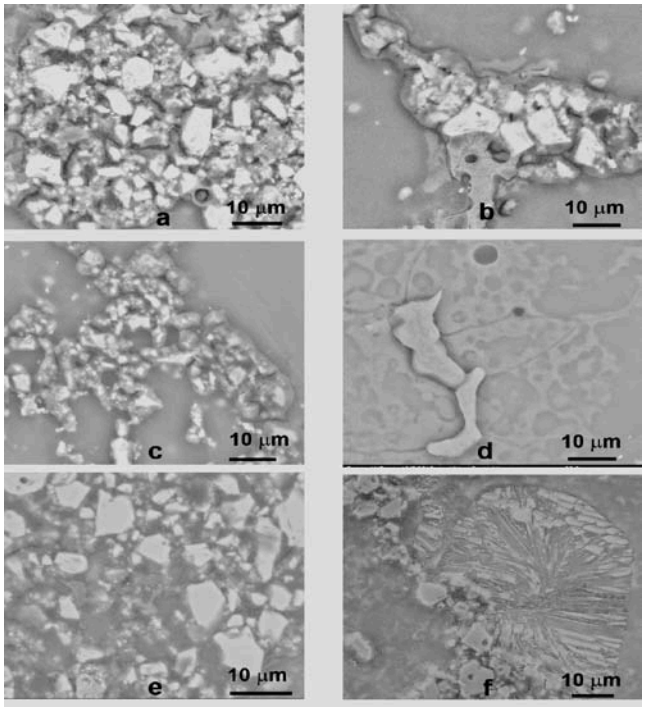

Fig. 3 Backscattered Electron Images (BSE) illustrating the impact of solution treatment and aging on the microstructure of Al-9 wt.% Al-10 Vol.% TiC. **a-b**) As cast, **c-d**) solution heat treated, and **e-f**) aged. (the corrections are bolded).

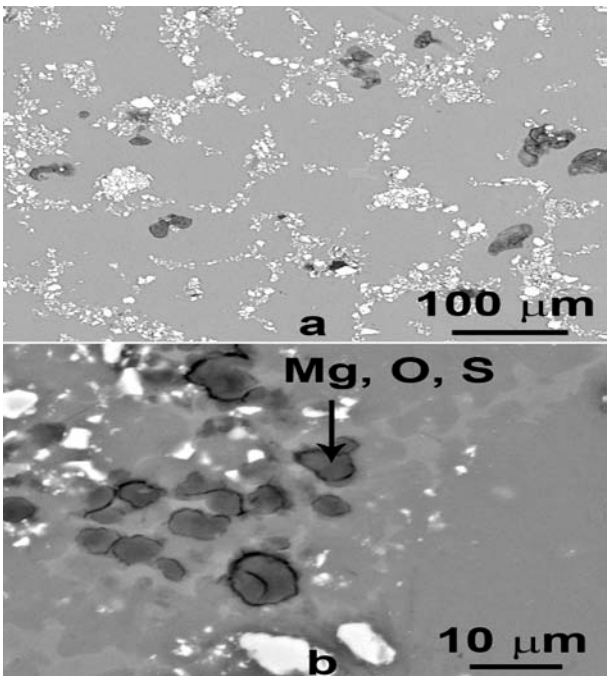

Fig. 4 BEI's of an upper region of the 10 vol. % TiC composite ingot showing the higher density of oxides.

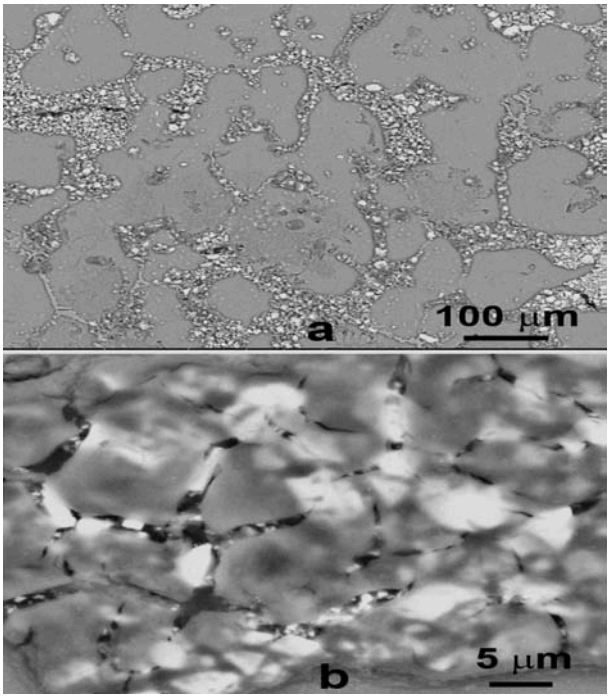

Fig. 5 BEIs of the 10 vol.% TiC composite rolled to 30% thickness reduction at 350oC. a) Low magnification view. b) Higher magnification of interdendritic regions showing microcracks.

Another issue is the uneven distribution of the TiC. While the majority of the billet microstructure is similar to that in Fig. 1c with a relatively even distribution of TiC particles in the interdendritic regions, there are regions in which the interdendritic regions contain continuous $Mg_{17}Al_{12}$ similar to that in Fig. 1b. Also, the regions of un-integrated TiC pellets such as that in Fig. 1a are, in some cases, quite large.

The oxygen in the interdendritic regions plays a central role in the ability of the Mg MMC's to undergo large thickness reduction during hot rolling. For example, a large number of microcracks can be seen in the interdendritic

regions (Fig. 5b) of the 10 vol.% TiC after rolling to 30% thickness reduction at 350°C. These micro-cracks can develop into a fracture as can be seen in Fig. 5a.

B. *Mechanical Properties*

Compression stress/strain curves illustrating the impact of the TiC reinforcements on an Mg-9 wt % Al matrix are shown in Fig. 6 and a summary of the compression results in Table 1. As can be seen from Fig. 6 and Table 1, the compressive yield strength increased from 110 MPa to 150, 310 and 380 MPa for 10, 20 and 30 vol.% TiC samples, respectively, while the compressive deformation to fracture decreased from 13% to about 2.5% for the 30 vol.% TiC sample. It is also apparent that increasing the volume fraction of the TiC reinforcement to 20% increased the compressive yield stress markedly whereas the additional increase to 30 vol.% increased the compressive yield only slightly.

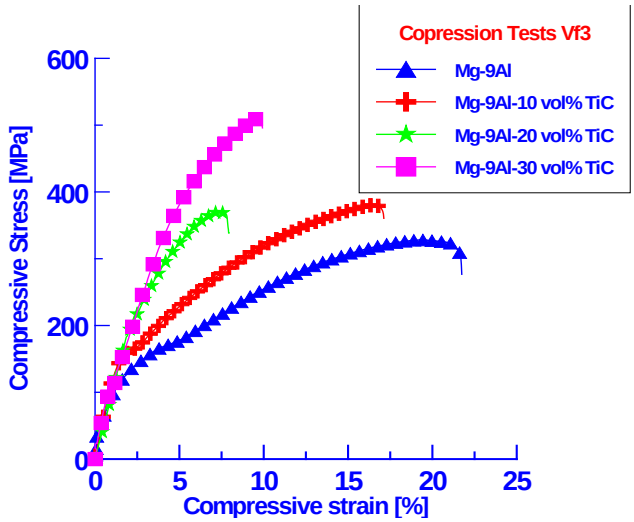

Fig. 6 Compressive stress/strain curves of Mg-9 wt % Al with and without different TiC volume fractions.

The Vickers microhardness of composites reinforced with different TiC volume fractions compared to the base Mg-9 wt % Al material in the as cast, solution heat treated and aged conditions are summarized in Table 2. As was discussed earlier, there were areas with concentrated amounts of TiC. Therefore, it is not surprising that we had 2 sets of values for each specimen corresponding to these differences. Increasing the vol. % TiC in the alloy increased the hardness as expected. The solution heat treatment reduced the microhardness values compared to the as-cast material, presumably due to the reduction of the $Mg_{17}Al_{12}$ interdendritic phases. Likewise, subsequent aging treatments increased the hardness due to precipitation in the Mg dendrites.

TABLE I
SUMMARY OF THE COMPRESSION TESTS FOR MG-9AL AS A FUNCTION OF THE VOL. % TIC

Alloy	Mechanical Properties		
	Yield Stress [MPa]	Ultimate Stress [MPa]	Compressive strain to fracture [%]
0 vol.% TiC	105	330	16.8
10 vol.% TiC	150	380	12.3
20 vol.% TiC	320	450	5.7
30 vol.% TiC	380	510	4.5

TABLE II.
MICROHARDNESS RESULTS FOR MG-9AL WITH DIFFERENT AMOUNTS OF TIC IN AS-CAST, SOLUTION HEAT TREATED AND AGED CONDITIONS

Condition	Microhardness (H_v)			
	0 vol.% TiC	10 vol.% TiC	20 vol.% TiC	30 vol.% TiC
As cast	72			
Solution treated	55	75 108	100 150	122 185
Aged	75	85 106	130 173	140 200

Abrasive wear resistance tests [17] showed the same tendency, namely, increasing TiC vol.% fraction decreased the wear depth in a manner inversely proportional to the hardness values.

IV. SUMMARY

Mg-based MMCs containing 10, 20 and 30 vol. % TiC were produced successfully by mixing TiC+Al powder compacts into liquid Mg. These composites were characterized in the as-cast condition and after solution treating and aging using SEM/EDS, microhardness and compression tests. The following results were obtained:

The Mg dendrites were composed of Mg with around 9 wt.% Al and, during solidification, the TiC particles were rejected to the interdendritic regions. In the interdendritic regions containing the TiC particles, Mg and Al oxides as well as the $Mg_{17}Al_{12}$ intermetallic phase were observed. In certain areas, lower percentages of TiC were observed and, in some cases, the interdendritic regions consisted solely of the $Mg_{17}Al_{12}$ phase. Solution heat treatment reduced the amount of $Mg_{17}Al_{12}$ and oxides, but did not eliminate them. Aging affected the Mg dendrites in a manner similar to the aging effect in Mg AZ91 alloys. Increasing the vol. fraction of TiC reduced the amount of the Mg dendrites without TiC.

Compression tests indicated an increase in the compressive yield strength as well as the maximum compressive strength while the compressive strain decreased with increasing TiC volume fractions. The microhardness also increased with increasing TiC volume fraction in the alloy. Solution heat treatment resulted in a decreased hardness whereas aging increased it to essentially the as-cast values.

There are two types of oxides in the Mg MMCs: small oxide particles in the interdendritic areas and relatively large oxides containing sulphur. The density of the larger oxides increased towards the top of the billet. Significantly, the small oxides clearly preclude large thickness reduction via hot rolling. Thus, it is clear that reducing the oxides in the interdendritic regions is important to improve overall properties and workability of the material

Finally, from a processing standpoint, the stirring system needs to be improved in order that all TiC can be distributed evenly throughout the ingot

ACKNOWLEDGEMENTS

This research was supported by the US Department of Energy under Award Number DE-EE0001100, the North American Die Casting Association and the China Scholarship Council of the Chinese Ministry of Education. The authors would like to thank Vforge Inc. and WPI for performing the semi-solid die casting trials and mechanical tests, respectively. The authors also wish to acknowledge the Electron

Microscopy Laboratory at CSM for making the equipment available or these studies.

REFERENCES

[1]. H. Friedrich and B. Mordike, Technology of magnesium and magnesium alloys in Magnesium Technology - Metallurgy, Design Data, and applications Springer–Verlag, 2006, 219-430.

[2]. E. Aghion and D. Eliezer, EDs. Magnesium 1997 - the First International Conference on Magnesium Science & Technology, The Dead Sea, Nov. 1997.

[3]. E. Aghion and D. Eliezer, EDs. Magnesium 2000 - the Second International Conference on Magnesium Science & Technology, The Dead Sea, Feb. 2000.

[4]. H. Choi, H. Konishi and X. Li," Effects of SiC nanoparticles on mechanical properties and microstructure of cast Mg-12wt.%Al-0.2wt.%Mn nanocomposites, in Magnesium Technology 2011, EDs: W. H. Sillekens, S. R. Agnew, N. R. Neelameggham, and S. N. Mathaudhu, TMS (The Minerals, Metals & Materials Society), 2011 pp. 447 to 452.

[5]. H.Z. Ye and X. Y. Liu, "Review of recent studies in magnesium matrix composites", Journal of Material Science, vol. 39, pp. 6153-6171, 2004.

[6]. H. Capel, S. J. Harris, P. Schulz and H. Kaufman, Mater. Sci. Techn. Vol. 16, 765, 2000.

[7]. Hausmann, C. Cayron, O. Beffort and S. Long, in 9th International Conference on Modern Materials and Technologies, CIMTEC'98, Florence, Italy, June 1998.

[8]. Diw Angi and I. W. Hall, J. Mater. Sci. vol. 27, p. 2093, 1992.

[9]. Y . Kagaw A and E.. Nakata , J. Mater. Lett. Vol. 11, p 176, 1992.

[10]. L. I. Lu, M. O. Lai, M. Gupta, B. W. Chua and A. Osman, J. Mater. Sci. vol. 35, p 5553, 2000.

[11]. S. Nimityongskul, N. Alba-Baena, H. Choi, M. Jones, T. Wood, M. Sahoo, R. Lakes, S. Kou, and X. Li, "Characterization of hot extruded Mg/SiC nanocomposites fabricated by casting", in Magnesium Technology 2011, Eds: W. H. Sillekens, S. R. Agnew, N. R. Neelameggham, and S. N. Mathaudhu, TMS (The Minerals, Metals & Materials Society), 2011, pp. 443 to 446.

[12]. G. Cao, H. Konishi and X. Li, "Mechanical properties and microstructure of Mg/SiC nanocomposites fabricated by ultrasonic cavitation based nanomanufacturing," Journal of Manufacturing Science and Engineering, vol. 130, pp. 31105-1 to 31105-6, 2008.

[13]. G. Cao et al., "Mg-6Zn/1.5%SiC nanocomposites fabricated by ultrasonic cavitation-based solidification processing," Journal of Materials Science vol. 43, pp. 5521–5526, 2008.

[14]. Z. Esen, "TiNi reinforced magnesium composites by powder metallurgy", in Magnesium Technology 2011, Eds: W. H. Sillekens, S. R. Agnew, N. R. Neelameggham, and S. N. Mathaudhu, TMS (The Minerals, Metals & Materials Society), 2011, pp. 457 to 462.

[15]. S. J. B. Reed, Electron Microprobe Analysis, Cambridge University Press, Cambridge, 1977.

[16]. W. Garrett, unpublished work, 2012

[17]. Jo, J. Nuechterlein, W. Garrett, A. Munitz, M.J. Kaufman , J.J. Moore, K. Young , C. Rice, M.M. Makhlouf , D. Apelian, and A. Monroe, SHS die-casting (SHS-DC) of magnesium metal matrix composites (MMCs), to be published in *NADCA, 241 Holbrook,* Wheeling, Illinois, 60090, 2012

Effective Parameters on Strength of Reinforced Clayey Sand

Amin chegenizadeh[#1], Hamid Nikraz[*2]

[#]Researcher at Curtin University, Civil Engineering,Curtin University,Perth,Australia

[*]Professor and head of civil engineering , Curtin University,Perth,Australia

[1]amin.chegenizadeh@curtin.edu.au; .nikraz@curtin.edu.au

***Abstract*-Soils and their related behavior has always been the subject of many studies. Recent researches show some interests in investigation of inclusion of randomly distributed fiber in soil. This study focuses on effect of fiber inclusion on the strength and other parameters of clayey sand composite material. The first part of this study is related to effective parameters on strength of the clayey sand composite with using natural fiber and plastic fiber with different fiber contents and length. UCS tests were carried out to investigate behavior of the composite under different condition. The fiber percentage varied from 0 % (for unreinforced samples) to 4% and fiber length varied from 8mm to 25mm. The fiber length and fiber content are found to play important roles in the strength of fiber reinforced composite. Furthermore it was observed that ductility of sample increased by fiber inclusion.**

Keywords- Component; UCS; Fiber; Strength

I. INTRODUCTION

Traditional ways of soil reinforcement involve the use of continuous planar inclusions (e.g. metallic strips, geogrids, geotexiles) in soil structures. The advances of these materials have usually been considered by an increase in their applications. The randomly short discrete fibers are easily added and mixed randomly with soil part, the same way as cement, lime or other additives. Some researches have been conducted on cement additive (Consoli et.al. 2009; Cai et.al 2006; Lorenzo and Bergado, 2004, Kaniraj et al. 2001) and can be used as a pattern of additive usage in soil. Fiber reinforced composite shows more ductility and smaller losses of peak strength i.e. compared to unreinforced material. Usage of fiber together with cement material can be useful as fiber inclusion helps composite to lose the brittle behavior gaining from being cemented. Therefore, application of fiber in soil composite is a practical solution in geotechnical engineering projects. On the other hand, due to the cost of engineering projects and also environmental issue related to the projects, natural fiber such as palm fiber is highly desirable as will be investigated in this paper. The main application of composite soil can be in embankment, sub-grade, sub-base, and slope stability problems. However, the data concerning the effects of fiber inclusion on the characteristics of compacted native or virgin soils are limited (Maher and Ho, 1993).

Working on different aspects of fiber inclusion in soils has been an interest all the time. Direct shear tests, unconfined compression tests and conventional triaxial compression tests have demonstrated that shear strength increases and post-peak strength reduces when discrete fibers are mixed with sandy soils (Al Refeai, 1991; Maher and Ho, 1994; Yetimoglu and Salbas, 2003; Tang et al., 2007, Chegenizadeh and Nikraz, 2011).

Fiber specifications including type, volume percentage, length, aspect ratio, modulus of elasticity, fiber orientation and also soil parameters have significant effects on the strength of composite samples. Moreover, fiber orientation has considerable influence on failure and strength (Jewell and Wroth, 1987; Micha1owski and Cermak, 2002; Gray and Ohashi (1983), Michlowski and Zhao (1999) and Zornberg (2002)).

However study on effects of fiber has been well investigated in sandy soil, research shortage is more considerable in clayey soil or mix of clay and sand. Therefore, more investigations on fiber inclusion in clayey composite are needed to be performed. As in practical engineering project, specifically geotechnical project strength has considerable effect on the design procedure; the first part of this study mainly focuses on changes in strength of composite clayey sand due to random plastic and natural fiber inclusion.

II. THEORETICAL BACKGROUND

Different approaches have been used so far to predict the behavior of reinforced soil. One of the most practical methods is Gray and Ohashi (1983) which investigate fiber inclusion in sandy soils with load transfer approach. This section focuses on these methods.

Gray and Ohashi (1983) presented a force equilibrium model based on the results of a series of direct shear tests performed on sands reinforced with fibers placed at defined orientations. The shearing of soils is assumed to cause fiber distortion along the shear plane, thereby mobilising its tensile resistance (Figure 1). The fiber-induced tension was calculated from the extension of fibers assuming that fibers length, interface friction and confining pressure are large enough to prevent pullout failure. In this case, the fiber-induced tension can be expressed as a function of fiber modulus, interface friction, fiber diameter and thickness of the shear zone as follows:

$$\sigma_t = \left(\frac{4\, e_f\, \tau_f\, z}{d_f}\right)(\sec\phi - 1)^{1/2} \qquad (1)$$

Where:

σ_t = tensile stress

τ_f =frictional resistance

ϕ = friction angle of soil

z =thickness of shear zoon

e_f = energy dissipated on the interface of a single fiber

d_f = equivalent diameter of single fiber

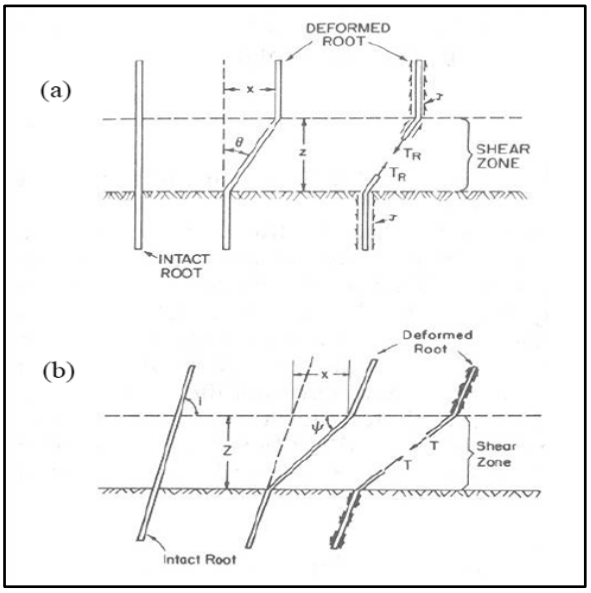

Fig. 1 Elastic fiber across the shear zone a) vertical fiber b) inclined fiber (Gray and Ohashi, 1983)

The contribution of the fiber-induced tension to the shear strength of the composite was determined with force equilibrium considerations, and was proposed by the following equation for fibers perpendicular to the shear plane:

$$\Delta S = t(\sin\theta + \cos\theta \tan\emptyset) \quad (2)$$

Where:

θ= angle of distortion of fiber (Figure 13)

t= mobilized tensile strength defined as:

$$t = (\frac{A_f}{A})\sigma_t \quad (3)$$

Where:

A_f = area of fiber in shear

A= area of failure plane

Equitation (2) can be expressed when the fibers are oblique as follows:

$$\Delta S = \sigma_t^{'}[(\sin(90-\psi) + \cos(90-\psi)\tan\emptyset)] \quad (4)$$

Where:

ψ= orientation angle of distorted fiber

$$\psi = \tan^{-1}[\frac{1}{(\frac{x}{z})+(\tan\ i)^{-1}}] \quad (5)$$

Where:

i = initial orientation of fiber

The fiber-induced tension force in terms of the fiber extension is calculated by Equation (1), which is valid only for extensible fiber with a frictional surface. Commonly used polymeric fibers have relatively high tensile strength and deformation modulus but relatively low interface friction. Therefore, this model may be inadequate when failure is governed by the pullout of fibers. In addition, this model requires determination of the thickness of the shear zone as an input parameter, which is difficult to compute (Li and Zornberg, 2003).

Maher and Gray (1990) further developed the model presented by Gray and Ohashi (1983) to apply it to randomly-distributed fibers by incorporating statistical concepts.The average number of fibers *Ns*, intersecting the unit area of the shear plane was defined as:

$$N_s = \frac{2\chi}{\pi {d_f}^2} \quad (6)$$

χ= fiber content

They also defined the tensile stress developed in a fiber as:

$$\sigma_t = 2(\sigma_n\ tan\,\delta)\frac{l_f}{d_f}, \sigma_n < \sigma_{ncrit} \quad (7)$$

$$\sigma_t = 2(\sigma_{ncrit}\ \tan\delta)\frac{l_f}{d_f}, \sigma_n > \sigma_{ncrit} \quad (8)$$

σ_n = confining stress on fiber

δ= angle of skin friction

l_f =total length of fiber

σ_{ncrit} = critical confinement corresponding to the break on the shear strength envelope

The shear strength increase ΔS, induced by fiber presence was obtained by substituting Equations (8) into (2), as follows:

$$\Delta S = N_s\left(\frac{\pi {d_f}^2}{4}\right)[2(\sigma_n\ \tan\delta)\frac{l_f}{d_f}](\sin\theta + \cos\theta\tan\emptyset)(\zeta), \sigma_n < \sigma_{ncrit} \quad (9)$$

$$\Delta S = N_s\left(\frac{\pi {d_f}^2}{4}\right)[2(\sigma_{ncrit}\ \tan\delta)\frac{l_f}{d_f}](\sin\theta + \cos\theta\tan\emptyset)(\zeta), \sigma_n > \sigma_{ncrit} \quad (10)$$

ζ= coefficient depends on sand parameter

As in the force equilibrium model proposed by Gray and Ohashi (1983), the model proposed by Maher and Gray (1990) still requires the thickness of shear zone as input, which is difficult to quantify. The expression of σ_{ncrit} was derived empirically (Maher, 1988) using the results from triaxial tests.

As the main previous studies are on sand, the current study in Curtin University considered new approach in using fibers types and materials to fully investigate the effects of fiber in clayey soils. As part of this research, the following section investigates clayey sand behaviour.

III. MATERIAL

Composite materials usually consist of two parts. The first part is soil part which can be dealt as normal soil. The second part is reinforcement part which can be made up of any material which helps soil to have better performance. As soils have relatively low tensile strength so that they are not able to transfer tensile forces through a foundation system. These forces can be transferred using geosynthetics materials - geogrids, geotextiles or geocomposites.

A. Soil Type

The soil type in this study was Western Australian sand. The properties of clay are presented in Table 1. The sand distribution curve is presented in Fig 1. The soil part was reconstituted in lab by using sand with 10% of kaolin clay.

TABLE1. CLAY PROPERTIES

No.	Type	
1	Soil type	Clay
2	Liquid Limit	49
3	Plastic Limit	23
4	Pl. Index	26

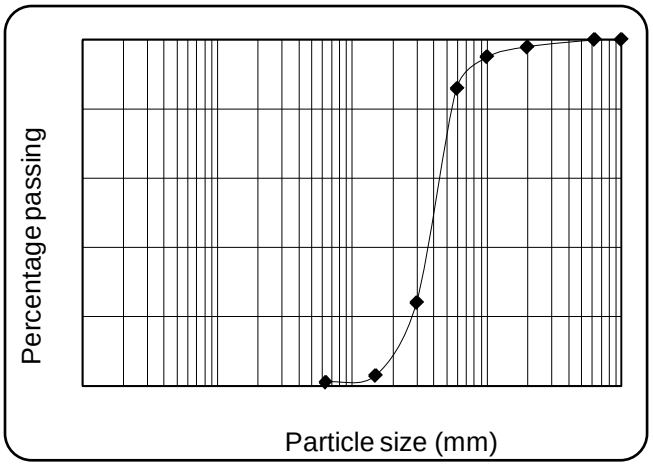

Fig. 1Sand particle distribution

B. Fiber Type

The natural fiber and plastic fiber has been used for this investigation. The natural fiber is available in Western Australia. This material can be easily found and prepared for industrial project. Being cost effective is the main advantage of this fiber. Figure 2 shows the natural used fiber. The second type of used fibers shown in Figure 3 was plastic fiber with great energy absorption capability. The main advantage of this plastic was its good interaction with soil part. The interlock forces were expected to be considerably higher than natural one due to skin friction. Therefore, the load transfer in case of plastic fiber was better than natural one.

Fig. 2 Natural fiber

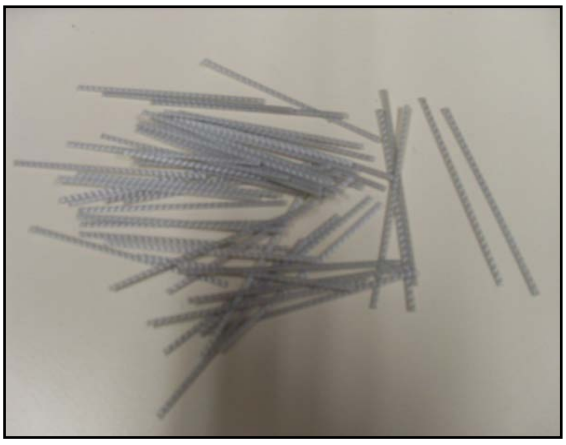

Fig. 3 Plastic fiber

IV. TEST PROGRAM

A series of UCS tests have been conducted to verify effect of fiber content on strength of composite clayey sand.

A. Unconfined Compression Test Principle

The aim of unconfined compression test is to obtain unconfined compressive strength of soil. This can be applied to fine grade and cohesive soil and will represent very fast response in practical condition as the test time is very quick in respect to confined one. This test is widely used for slope stability and embankment dam applications.

B. Equipment

- Unconfined compression testing machine (Triaxial Machine) as shown in Figure 4
- Specimen preparation equipment
- Sample extruder
- Balance

Fig. 4Triaxial machine

C. Sample Preparation

The samples were prepared by mixing clayey sand and four percentage of fiber. Specimen preparation method was the standard compaction method, which was used in an ongoing experimental research on fiber-reinforced clayey sand at Curtin University. The soils were first oven-dried. The dry soils were then crushed using a hammer. A mixer was used to thoroughly mix the soils with water to obtain the desired water moisture content for compaction. The mixing of soil with fibers was performed mostly by hand rather than by mixer because mixer caused the fibers to tangle or break. The fiber-soil mixture was placed in a closed container for 24 hours after mixing was completed. A split mold and a specific hammer were used to compact the specimen. The specimens were prepared in different fiber contents (i.e. 0.6%, 1.5%, 4%) and different fiber lengths (aspect ratio) which were 8mm, 20mm and25mm.

V. TEST PROCEDURE

1. The specimens were prepared in the laboratory with 90% compaction effort, special care was taken during this process
2. The size of samples were checked to be suitable for the test purpose
3. The samples were put for 24 hours in geotxtile and packed

4. Special attention was paid to preventing any moisture loose
5. The samples were put in triaxial base without any confinement pressure
6. According to ASTM, 1.27 mm/min was applied through the tests
7. The data were collected automatically
8. The stress-strain curve plot was used for modulus elasticity investigation

VI. RESULTS AND DISCUSSION

A series of UCS tests were conducted on fiber reinforced samples. Fiber parameters were changed during this study to evaluate the effect of each fiber parameter. (i.e. type, content and length). This section focuses on effect of each parameter.

A. *Effect of Fiber Type*

Two types of fiber were used in this research (i.e. plastic and natural). The results are presented in following figures. The results showed the difference in strength due to change in fiber material.

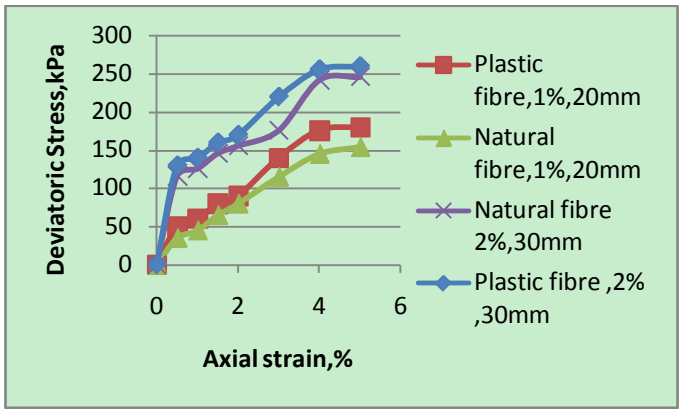

Fig. 5 Effect of fiber type on strength of clayey sand composite

The change in fiber material proved that the plastic fiber increased the strength of reinforced samples more than natural fiber. The main reasons can be considered as interlock forces between soil and fiber as the adhesion of soil part and fiber worked more proper than the natural one.

B. *Effect of Fiber Content*

The effect of fiber content was well investigated as the UCS tests were run for different fiber contents and constant length and type. The fiber length is kept at 8mm and plastic fiber is used for these tests. The Fig. 6 shows the effect of fiber content on strength of the samples.

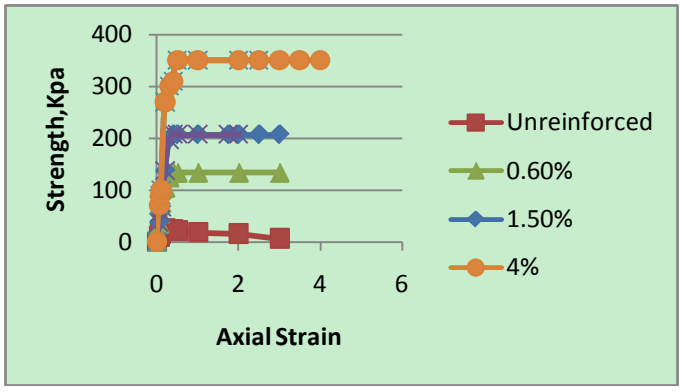

Fig. 6 Effect of fiber content on strength of clayey sand composite (at 8mm)

C. *Effect of Fiber Length*

The effect of fiber length was well investigated as the UCS tests were run for different fiber length and constant content and type. The fiber type is kept as plastic fiber and the fiber content as 0.6%. The Fig. 7 shows the effect of fiber content on strength of the samples.

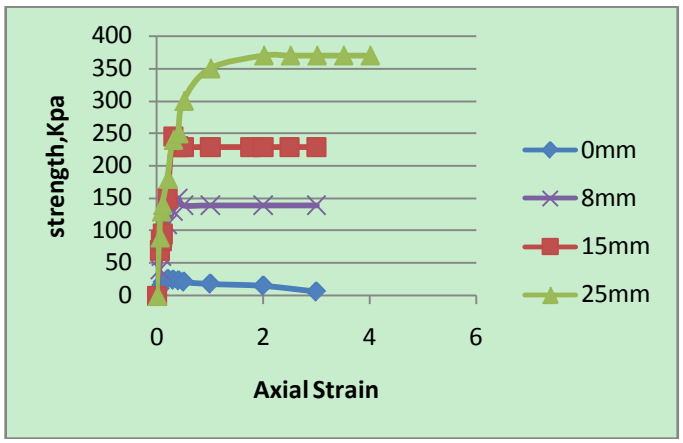

Fig. 7 Effect of fiber length on strength of clayey sand composite (at 0.6%)

VII. CONCLUSION

A series of UCS tests were conducted to examine the effect of fiber content, length and fiber type. The results showed that:

- These three parameters (i.e. fiber content, length and type) affected the performance and strength of composite clayey sand significantly.
- The tests proved that with the increase in fiber content, the strength increased considerably. The strength peak increased by six times in case of increasing in fiber content by four times.
- The results also proved that increasing in fiber length increased the strength of the composite. As an instance when fiber length increased from 8 mm to 25mm, the peak increased from 125 kpa to 340 kpa.
- During this research, the effects of fiber type (i.e. plastic fiber and natural fiber) were investigated. The results proved that increasing in strength of composite material was more considerable in case of plastic fiber compared to natural one. The main reason can be found as skin friction difference as the interlock forces for plastic fiber was more than natural one.

ACKNOWLEDGMENT

Authors would like to thank Curtin laboratory staff for their kind assistance.

REFERENCES

[1]. Akbulut, S., Arasan, S. and Kalkan, E. (2007) “Modification of clayey soils using scrap tire rubber and synthetic fibers”, Journal of Applied Clay Science 38, 23-32.

[2]. Al Refeai, T.O. (1991) “Behaviour of granular soils reinforced with discrete randomly oriented inclusions”, Journal of Geotextiles and Geomembranes 10, pp. 319–333.

[3]. Cai, Y., Shi, B., Charles, W.W. Ng. & Tang, C. (2006)” Effect of polypropylene fiber and lime admixture on engineering properties of clayey soil”, Engineering Geology 87, 230– 240.

[4]. Chegenizadeh, A. and Prof.Hamid Nikraz , “Modulus of Elasticity of Reinforced Clay” , Journal of Advanced Materials Research, 261-263, 969-973, DOI 10.4028/www.scientific.net/AMR.261-263.969

[5]. Chegenizadeh, A. and Prof.Hamid Nikraz ,"Permeability Test on Reinforced Clayey Sand", Journal of World Academy of Science, Engineering and Technology 78 2011, 130-133

[6]. Chegenizadeh, A. and Prof.Hamid Nikraz, "Automated Shear Test on Reinforced Clayey Sand", Journal of Advanced Materials Research, 261-263, 1019-1023, DOI: 10.4028/www.scientific.net/AMR.261-263.1019

[7]. Chegenizadeh, A. and Prof.Hamid Nikraz ,"Investigation on Compaction Characteristics of Reinforced Soil", Journal of Advanced Materials Research, 261-263, 964,10.4028/www.scientific.net/AMR.261-263.964

[8]. Chegenizadeh, A. and Prof.Hamid Nikraz ,"Shear Test on Reinforced Clay", Journal of Advanced Materials Research, 250-253, 3223, DOI: 10.4028/www.scientific.net/AMR.250-253.3223

[9]. Chegenizadeh, A. and Prof.Hamid Nikraz ,"Study on Modulus of Elasticity of Reinforced Clay", Journal of Advanced Materials Research, 243-249, 5885, DOI: 10.4028/www.scientific.net/AMR.243-249.5885

[10]. Chegenizadeh, A. and Prof.Hamid Nikraz ,"Investigation on Strength of Fiber Reinforced Clay", Journal of Advanced Materials Research, 261-263, 957, 957-963, DOI:10.4028/www.scientific.net/AMR.261-263.957

[11]. Chegenizadeh, A. and Prof.Hamid Nikraz ,"Geotechnical Parameters of Composite Soil ", Journal of Advanced Materials Research, Advanced design technology ,1651,2011

[12]. Chegenizadeh, A. and Prof.Hamid Nikraz ,"Composite Soil: Fiber Inclusion and Strength", Journal of Advanced Materials Research,1646, 2011, Journal in press

[13]. Chegenizadeh, A. and Hamid Nikraz ,Interaction of soil and short fiber, , ASTM digital library,2011,In press

[14]. Chegenizadeh, A. and Hamid Nikraz, Composite Clayey Sand and Short Fiber, Advanced Materials Research Journal, In press

[15]. Consoli, N.C., Vendruscolo, M.A., Fonini, A. and Dalla Rosa, F. (2009) "Fiber reinforcement effects on sand considering a wide cementation range", Geotextiles and Geomembranes 27, pp. 196–203.

[16]. Freitag, D.R. (1986) "Soil randomly reinforced with fibers", Journal of Geotechnical Engineering ASCE 112 (8), pp. 823–826.

[17]. Gray, D. H. (1970) "Role of woody vegetation in reinforcing soils and stabilizing slopes" Proc., Symp. on Soil Reinforcement and Stabilizing Techniques, pp. 253-306.

[18]. Gray, D.H. and Ohashi, H. (1983) "Mechanics of fiber reinforcement in sand", Journal of Geotechnical Engineering ASCE 109 (3), pp. 335–353.

[19]. Gray, D.H. and Alrefeai, T. (1986) "Behavior of fabric-reinforced versus fiber-reinforced sand", Journal of Geotechnical Engineering ASCE112 (8), pp. 804–820.

[20]. Gregory, G. H. (1999) "Theoretical shear-strength model of fiber-soil composite." Proc., ASCE Texas Section Spring Meeting, ASCE, Longview, Tex., pp.1–10.

[21]. Kaniraj, S. R., Havanagi, V. G. (2001). "Behaviour of cement-stabilized fiber reinforced fly ash-soil Mixtures", Journal of Geotech. and Geoenvironmental. Engineering 127 (7), pp. 574-584.

[22]. Li, C., and Zornberg, J.G. (2003) "Validation of discrete framework for fiber-reinforcement", Proceedings of the 2003 North American Conference on Geosynthetics. Winnipeg, Canada, pp. 285-293

[23]. Lorenzo, G. A. and Bergado, D. T. (2004). "Fundamental parameters of cement-admixed clay – New approach." Journal of Geotechnical and Geoenvironmental Engineering, Vol. 130, No. 10, pp. 1-9.

[24]. Maher, M.H. and Gray, D.H. (1990) "Static Response of sands reinforced with randomly distributed fibers", Journal of Geotechnical Engineering ASCE 116 (11), pp. 1661–1677.

[25]. Maher, M.H. and Ho, Y.C. (1994) "Mechanical properties of kaolinite/fiber soil composite", Journal of Geotechnical Engineering 120 (8) (1994), pp. 1381–1393

[26]. Michalowski, R. L., Cermak, J. (2002), "Strength anisotropy of fiber-reinforced sand". Computers and Geotechnics, Vol. 29, No. 4, pp. 279-299.

[27]. Michalowski, R.L. and Zhao. (1999) "A. Failure of unidirectionally reinforced composites with frictional matrix", Journal of Engineering Mechanics ASCE122 (11), pp. 1086–1092.

[28]. Nataraj, M. S., Mcmanis, K. L. (1997), "Strength and deformation properties of soils reinforced with fibrillated fibers". Geosynthetics Int., Vol. 4, No. 1, pp. 65-79.

[29]. Ozkul, Z. H., and Baykal, G. (2007) "Shear behavior of compacted rubber fiber–clay composite in drained and undrained loading.", Journal of Geotechnical and Geoenvironmental EngineeringASCE 7, pp. 767–781.

[30]. Park, S.S. (2009) "Effect of fiber reinforcement and distribution on unconfined compressive strength of fiber-reinforced cemented sand", Geotextiles and Geomembranes 27, pp. 162–166.

[31]. Puppala, A. J. and Musenda, C. (2000) "Effects of fiber reinforcement on strength and volume change in expansive soils", Transportation Res. Rec.(1736), pp.134- 140.

[32]. Ranjan, G., Vasan, R.M. and Charan, H.D. (1996) "Probabilistic analysis of randomly distributed fiber-reinforced soil", Journal of Geotechnical Engineering ASCE122 (6), pp. 419–426.

[33]. Sivakumar Babu, G.L., Vasudevan, A.K. and Haldar, S. (2008) "Numerical simulation of fiber-reinforced sand behaviour", Geotexiles and Geomembranes26, pp. 181–188.

[34]. Sivakumar Babu, G.L., Vasudevan, A.K. and Haldar, S. (2008) "Numerical simulation of fiber-reinforced sand behaviour", Geotexiles and Geomembranes 26, pp. 181–188.

[35]. Tang, C.S., Shi, B., Gao, W., Chen, F.J. and Cai, Y.S. (2007) "strength and mechanical behavior of short polypropylene fiber reinforced and cement stabilized clayey soil", Geotextiles and Geomembranes25 (3), pp. 194–202.

[36]. Yetimoglu, T. and Salbas, O. (2003) "A study on shear strength of sands reinforced with randomly distributed discrete fibers", Geotextiles and Geomembranes 21 (2), pp. 103–110.

[37]. Ziegler, S., Leshchinsky, D., Ling, H. I., and Perry, E. B. (1998)" Effect of short polymeric fibers on crack development in clays". Soils and Foundations, Vol. 38, No. 1, pp. 247-253.

[38]. Zornberg, J. G., Cabral, A. R. and Viratjandr, C. (2004) "Behavior of tire shred-sand mixtures", Canadian Geotechnical Journal 41 (2), pp. 227–241.

[39]. Zornberg, J. G. (2002)" discrete framework for limit equilibrium analysis of fiber-reinforcement", Geotechnique Journal 52 (8), pp. 227–241.

Viscoelastic Properties and Reinforcement Performance of the MoS_2 Nanotubes–polymer Composite

A. Jelen[1], V. Bukošek[2], J. Dolinšek[1,3,4,*]

[1]Solid State Physics Department, J. Stefan Institute, Ljubljana, Slovenia

[2]Department of Textiles, Faculty of Natural Sciences and Engineering, University of Ljubljana, Slovenia

[3]Faculty of Mathematics and Physics, University of Ljubljana, Slovenia

[4]EN–FIST Centre of Excellence, Slovenia

jani.dolinsek@ijs.si .

***Abstract*-We present viscoelastic properties and reinforcement performance of a polymer nanocomposite containing MoS_2 nanotubes. The MoS_2 nanotubes are mechanically strong and flexible, behaving as super shock absorbers and exceptional lubricants with very low friction coefficient and excellent wear resistance. Using Dynamic Mechanical Analysis, we have defined viscoelastic properties (the storage modulus E', the loss modulus E'', the phase lag δ and the length l) of the MoS_2–polymer nanocomposite coatings with different nanotubes concentrations. The glass transition temperature of the nanocomposites has shifted by $\Delta T_g \approx 10^0$C towards higher temperatures. The $\tan\delta$ peak temperature T_δ and the temperatures T_{lmax} and T_{lmin} of the maximum elongation/contraction have shifted towards higher temperatures by the same amount. The main benefit of the MoS_2 nanotubes addition is a significant increase of the storage modulus E' within the temperature range suitable for mechanical loading, being roughly a factor of 2 larger than E' of the base coating without the MoS_2 nanotubes.**

Keywords-Nanocomposites; MoS_2; nanotubes; Dynamic Mechanical Analysis

I. INTRODUCTION

Polymer matrix-based nanocomposites are involved in a range of applications including material reinforcement, barrier to permeation, flammability resistance, polymer blend compatibilization, biomedical tissue engineering, drug delivery/release applications, fuel cells, electronics, photovoltaics, sensors, antimicrobial and cosmetic applications [1]. The addition of nanosized particles to the polymer matrix results in a change of the glass transition temperature T_g, the degree of crystallinity and the crystallization rate, which affect the properties of the nanocomposite in a fundamental way. In the reinforcement application [2], a common reason for adding nanofillers to polymers is to increase the Young's modulus or stiffness, the strength and the toughness of the nanocomposite. Nanocomposite has also a weight advantage over the conventional glass-fiber reinforced composite. Moreover, while fibers reinforce only along a single axis in the direction of their alignment, nanoparticles generally reinforce in all directions. Surface finish of the nanocomposite is much better than that of the glass fiber, owing to the nanometer size of the particles. One of the disadvantages of adding fillers is that they generally decrease the ductility of polymers, i.e. elongation at break. The reduced ductility is more severe when the polymer matrix is below its glass transition, whereas it is less dramatic above T_g. Better reinforcement results are generally obtained above T_g as it is easier to reinforce softer matrices.

There are four main system requirements for effective reinforcement of a nanocomposite by tube-type nanofillers (e.g. nanotubes, nanorods, nanoropes and nanofibers). These are:

(1) Large aspect ratio *l/D*, where *l* is the tube length and *D* its external diameter. In order to maximize the composite stiffness and strength, long tubes are generally required. However, long tubes are hard to disperse properly, so that one is faced with a trade-off. Similarly, low-diameter nanotubes give rise to greater surface area allowing maximization of interaction with the matrix. However, if the diameter gets too small, the maximum nanotube loading level (stress transfer) will be compromised. For these reasons there exist optimum diameter and length, with *l* typically of the order of a few μm and *D* of the order of 100 nm;

(2) Good dispersion, where the nanotubes must be uniformly dispersed to the level of isolated nanotubes individually coated with polymer. This is imperative in order to achieve efficient load transfer to the nanotube network and a uniform stress distribution. Any aggregation of the nanotubes due to poor dispersion is accompanied by a decrease in strength and modulus;

(3) Alignment is less crucial issue. For perfect alignment, the composite modulus is theoretically a factor of five larger than for random orientation. While alignment is necessary to maximize the strength and stiffness, aligned composites have very anisotropic mechanical properties, which may need to be avoided in bulk samples;

(4) the most important requirement for a nanotubes-reinforced composite is that external stresses applied to the composite as a whole are efficiently transferred to the nanotubes, allowing them to take a disproportionate share of the load. Upon application of an external stress, σ, the polymer matrix undergoes greater strain, ε, than the nanotube, because the nanotube modulus E_{NT} is much larger than the matrix modulus E_m and $\sigma=E\varepsilon$. The result is that a shear stress field can be very large adjacent to the nanotube. It is this matrix shear stress at the interface that controls stress transfer to the nanotube. At some critical value of the interfacial shear stress, either the matrix in the vicinity of the interface or the matrix-nanotube bond will rupture, which results in debonding and consequent mechanical failure of the

nanocomposite. The critical value of the interfacial shear stress governs the maximum stress transfer to the nanotube. Good adhesion of the nanotubes to the matrix is thus necessary for efficient stress transfer.

Carbon nanotubes turned out to be superior reinforcement filler material for improving stiffness/strength of the nanocomposites [2]. Other nanofiller materials incorporated in polymer composites were also used for property enhancement [1]. These include exfoliated clays for improved stiffness/strength and permeability barrier, multi-walled carbon nanotubes for improved electrical conductivity, carbon black for improved strength, wear and abrasion, silver nanoparticles for antimicrobial application and electrically conductive ink and silica nanoparticles for viscosity control. In this paper we present processing and viscoelastic properties of a polymer nanocomposite by using MoS_2 nanotubes [3,4] as the filler material. The MoS_2 and the related WS_2 nanotubes and fullerene-like nanoparticles possess a rare combination of being mechanically very strong and flexible [5]. The Young's modulus of the MoS_2 nanoropes (composed of several nanotubes) was estimated to have its lower limit at 120 GPa [5]. The MoS_2 and WS_2 nanotubes behave as exceptional lubricants [6, 7], either solid-state or as additives to lubricating fluids, with very low friction coefficients (between 0.008 and 0.01) [8] and excellent wear resistance. The MoS_2 and the WS_2 nanoparticles were also shown to act as super shock absorbers at very high pressures [9], surviving shocks as high as 25 GPa. MoS_2 nanotubes can store relatively large amounts of hydrogen [10], having gaseous storage capacity of 1.2 wt. % hydrogen. The MoS_2 and WS_2 nanomaterials were also used in electronic devices [11] and as catalysts [12]. Their superior mechanical/tribological properties make them promising nanofillers in polymer-based nanocomposites for the reinforcement application. Using Dynamic Mechanical Analysis (DMA), we present viscoelastic properties of the MoS_2 nanotubes–polymer composite as a function of the temperature and concentration of the nanotubes.

II. NANOCOMPOSITE PROCESSING

The commercial MoS_2 nanotubes were supplied by Nanotul, d.o.o., Slovenia. The SEM secondary-electron micrograph of the nanotubes is shown in Fig. 1. The tube lengths range from a few up to 15 μm, whereas their diameters are from 100 to 400 nm, assuring close to optimal aspect ratio *l*/D. A small fraction of smaller rods with lengths in the submicron range and diameters of about 100 nm is present as well. The small rods are attached to the larger ones. The nanotubes are flexible and can bend and twist. In some cases, the growth direction has changed discontinuously, producing zigzag structures. The nanotube edges are not perfectly closed, allowing better adhesion of the polymer because of more rough contact surface. The as-grown nanotubes show tendency to attach parallel to each other, forming sheaves of three or more nanotubes bound together.

In the first step of the nanocomposite processing, solvents, methacrylate monomers for polymerization, additives for light stabilization and UV absorption and a catalyst were added together. In the second step, MoS_2 nanotubes were added in volumetric fractions 0, 1, 3, 6, 12 and 15 vol. %, followed by ultrasonication for fine dispersion. The hardening step involved addition of hexamethylene diisocyanate for polymerization. All processing was performed at controlled room temperature (RT).

Nanocomposite coatings were produced on aluminum holders of 25 mm diameter for the SEM microscopy, wherefrom they could be later removed for testing with DMA. Freshly mixed components of the nanocomposite were deposited drop by drop with constant mixing. The coatings were left for 24 hours at RT for polymerization and solvents evaporation. The thickness of the coatings was typically about 280 μm. Six coatings were produced altogether. The reference coating without the MoS_2 addition is denoted as the *base* in the following. The five nanocomposite coatings containing MoS_2 nanotubes are denoted as the base + vol. % of MoS_2 addition (i.e., base + 1 %, base + 3 %, etc.).

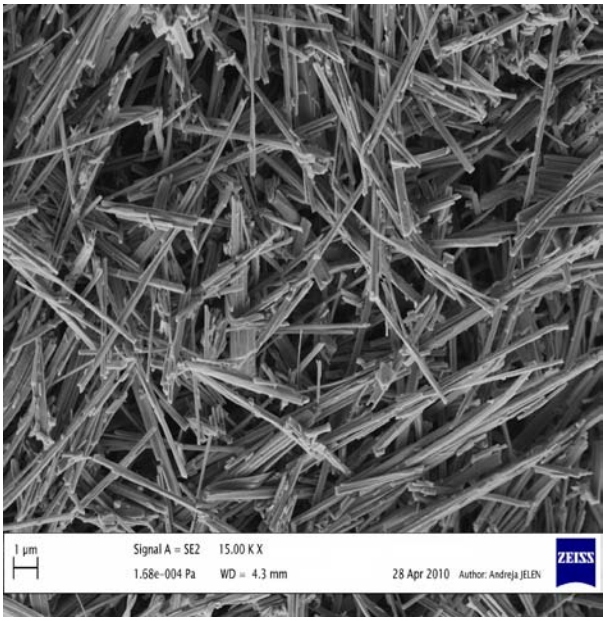

Fig. 1 SEM secondary-electron micrograph of the MoS_2 nanotubes

III. NANOCOMPOSITE CHARACTERIZATION BY MICROSCOPY TECHNIQUES

The microscopy characterization of the nanocomposite coatings was performed by Light Microscopy (LM) using optical stereo microscope Leica EZ4D with integrated CCD camera and imaging software Leica Microsystems LAS EZ, Scanning Electron Microscopy (SEM) using field-emission SEM Karl Zeiss Supra 35 VP and Transmission Electron Microscopy (TEM) using JEOL JEM-2100 TEM.

A. LM Characterization

Fig. 2 shows LM images of the six investigated coatings. The base coating is transparent, so that the shiny polished aluminum holder surface is seen underneath (Fig. 2a). The lines are scratches on the polished holder surface. By adding MoS_2 nanotubes, the coatings are gaining in optical density. At 1 % addition (Fig. 2b), the coating is still mostly transparent. Majority of the nanotubes have organized into groups of different sizes from sub-micron up to 100-μm diameter (observed as black spots) that are distributed evenly over the sample. The base + 3 % coating is almost opaque (Fig. 2c). The groups of nanotubes are smaller and their distribution is denser, approaching more homogeneous distribution. A few scratches on the holder remain visible. The base + 6 % (Fig. 2d), base + 12 % (Fig. 2e) and base + 15 % (Fig. 2f) coatings have similar appearance, showing full coverage of the holder with no transparency any more, as a consequence of a homogeneous distribution of the nanotubes.

Inhomogeneities of the nanotubes distribution on the scale below the LM resolution of about 200 nm cannot be excluded.

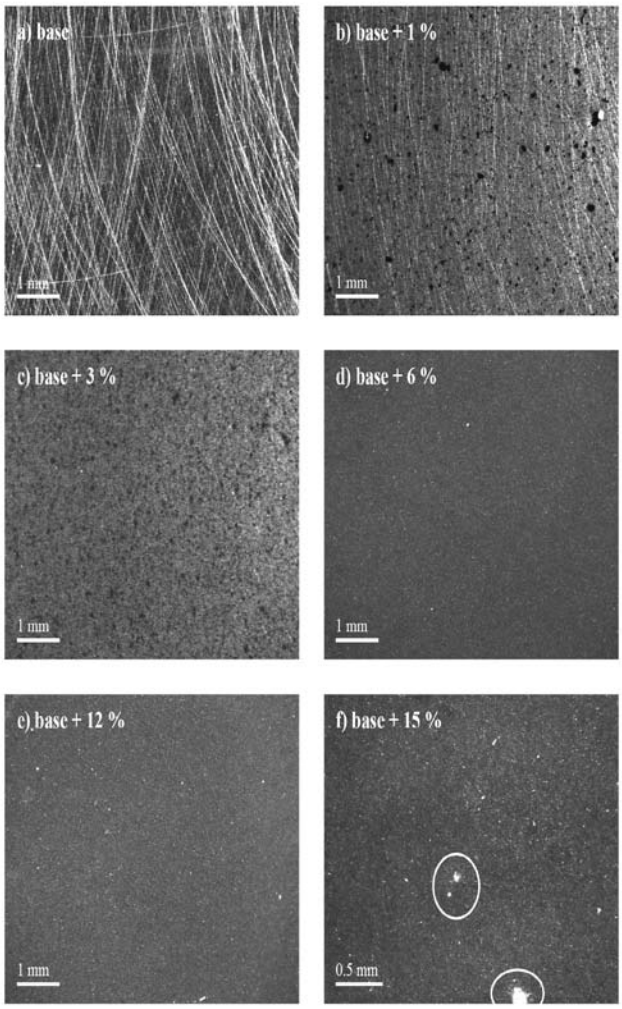

Fig. 2 LM images of the six investigated coatings, denoted as the base + vol. % of the MoS_2 nanotubes addition. (a) base, (b) base + 1 %, (c) base + 3 %, (d) base + 6 %, (e) base + 12 %, (f) base + 15 %. The magnification in the panel (f) is twice larger than in the other panels. White spots encircled in the panel (f) are due to light reflection.

The LM results show that the MoS_2 nanotubes disperse homogeneously over the nanocomposite coating at the concentration level of 6 % and higher. At 6 %, the coating is already totally opaque, whereas 15 % nanotube addition causes the shiniest surface.

B. SEM Characterization

The SEM imaging of the coatings was performed on their top surface and the cross section. Representative images of the base + 6 % coating are shown in Fig. 3. The cross section image in Fig. 3a shows good dispersion of the nanotubes at the level of isolated tubes individually coated with polymer. Homogeneous dispersion and good adhesion of the polymer to the nanotubes are in favor of efficient transfer of the external stresses to the nanotube system in the composite reinforcement application. The image of the top surface (Fig. 3b) shows excellent surface finish with negligible roughness on the 10 μm scale.

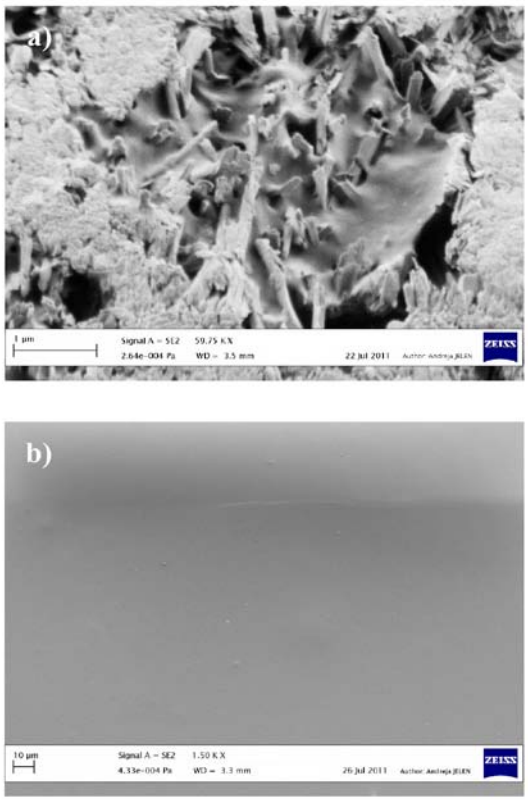

Fig. 3 SEM images of the base + 6 % coating: (a) cross section, (b) top surface.

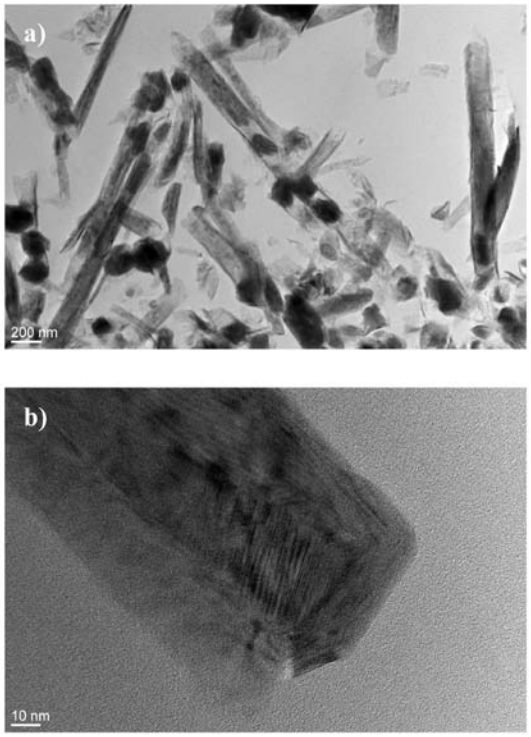

Fig. 4 (a) TEM image of the base + 12 % coating, showing fullerene-like MoS_2 nanoparticles inside the MoS_2 "mama-tubes". (b) Detail of the MoS_2 nanotube on a 10 nm scale, showing its crystallinity.

C. TEM Characterization

The TEM images of the base + 12 % coating (to be considered representative of all coatings) are shown in Fig. 4. On the scale of several 100 nm (Fig. 4a) we observe that some MoS_2 nanotubes contain nanoparticles inside, observed as dark spherical-like spots. Such tubes are known as "mama-

tubes" [13, 14] and contain lumps of the same material, MoS_2 fullerene-like nanoparticles in this case. The hollow mama-tubes thus act as nanopods. Fullerenes are not observable in all nanotubes. In some cases fullerenes have fallen out of the tubes and form constituting part of the nanocomposite. It is these MoS_2 fullerene-like nanoparticles that act as the super shock absorbers [9], indicating that our nanocomposite coatings might possess the shock-absorbing property. In Fig. 4b, the crystallinity of the MoS_2 nanotube can be observed on the nm scale.

The above presented characterization of the nanocomposite coatings with LM, SEM and TEM microscopy techniques has shown that the MoS_2 nanotubes disperse homogeneously and isotropically within the polymer matrix to the level of isolated tubes individually coated with polymer. SEM imaging of the nanocomposite cross section indicates good adhesion of the nanotubes to the polymer matrix. Together with superior mechanical properties of the MoS_2 nanotube fillers and the presence of fullerene-like MoS_2 nanoparticles, this makes the MoS_2–polymer nanocomposite promising candidate for the reinforcement application.

IV. DYNAMIC MECHANICAL ANALYSIS OF THE NANOCOMPOSITE

DMA is a technique suitable for studying viscoelastic behavior of polymers. A sinusoidal displacement (strain ε) is applied to the material and the resulting force (stress σ) is measured. For a perfectly elastic solid, the strain and stress are in phase. For a purely viscous fluid, there is a 90° phase lag of strain with respect to stress. Viscoelastic polymers are characterized by a phase lag somewhere in between these values.

For sinusoidal stress $\sigma = \sigma_0 \sin(\omega t + \delta)$ and strain $\varepsilon = \varepsilon_0 \sin \omega t$, where δ is the phase lag, the tensile storage modulus E', the loss modulus E'' and the tan δ are defined as

$$E' = \frac{\sigma_0}{\varepsilon_0} \cos \delta, \quad (1)$$

$$E'' = \frac{\sigma_0}{\varepsilon_0} \sin \delta, \quad (2)$$

$$\tan \delta = \frac{E''}{E'}. \quad (3)$$

The storage modulus E' measures the stored energy, representing the elastic portion, whereas the loss modulus E'' measures the energy dissipated as heat due to internal friction, representing the viscous portion. One important application of DMA is the measurement of glass transition temperature T_g of polymers. Above T_g, the material has rubbery properties and the stiffness of the material drops dramatically with an increase in viscosity. At T_g, the storage modulus decreases strongly and the loss modulus reaches a maximum. Incorporation of reinforcing fillers into the polymer generally changes T_g and increases the storage modulus at an expense of limiting the loss tangent peak height.

DMA experiments were performed on TA Instruments Q800 apparatus in the temperature range from –50 °C to 100 °C. Testing was done in tensile mode. Coatings samples were cut in the shape of ribbons with lengths around 20 mm and widths from 4 to 5mm. The starting clamping length was from 8.5 to 10mm. The clamping stress was 5 psi and the load was 125 % of the drive force. In this way, the samples were flat and leveled during the whole experiment, making no folds when exposed to sinusoidal deformation. The length of the samples was measured constantly during the tests. At the starting temperature, the length was measured firstly and this was the clamping length. At each temperature, the momentary length was used for the modulus correction because of heating. Therefore, the modulus values do not base on the clamping length, but on momentary length and computer calculations, assuring more accurate values of the modulus. The DMA tensile test was performed at $\nu = 1$ Hz frequency and 10 μm deformation amplitude.

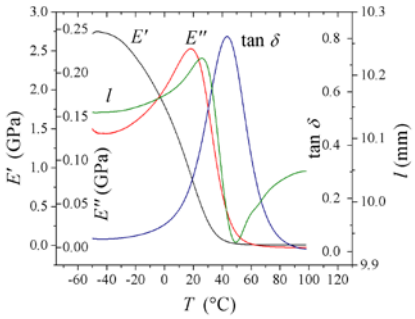

Fig. 5 (Color online) Viscoelastic properties of the base coating determined by DMA in the temperature range between –50 and 100°C: the storage modulus E', the loss modulus E'', the tan δ and the length *l*.

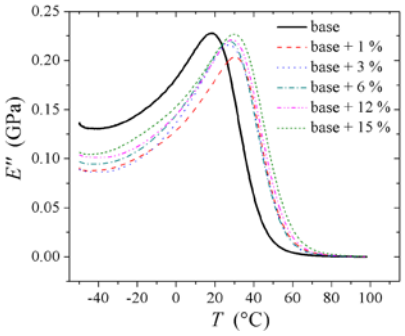

Fig.6 (Color online) Temperature-dependent loss modulus E''of the investigated coatings. The samples are denoted as the base + vol. % of the MoS_2 nanotubes addition

A. *Viscoelastic Properties of the Base Coating*

In the first set of the DMA experiments, viscoelastic properties of the base coating were defined as a function of temperature. The resulting storage modulus E', loss modulus E'', tan δ and length *l* are shown on the same graph in Fig. 5. The maximum in E'' occurs at the temperature 18.4 °C, which represents the glass transition temperature T_g of the base at the employed frequency of 1 Hz. The storage modulus drops drastically as the material goes from the hard glassy to a rubbery state, from the maximum value of E'_{max} = 2.75 GPa at T = –50 °C to the value at T_g of E'_{Tg} =0.88 GPa, whereas the RT value at T = 25 °C is E'_{RT}= 0.53 GPa. The loss modulus value at T_g amounts E''_{Tg} = 0.23 GPa, whereas the RT value is E''_{RT} = 0.21 GPa. The tan δ curve shows maximum at the temperature T_δ= 42.9 °C and the maximum phase lag at T_δ amounts $\delta_{T\delta}$= 39°. T_δ defines one end of the temperature range over which the polymer can be used, called the operating range of the polymer. If the strength and stiffness are required, T_δ is the upper limit, whereas for rubber-like application, it is the lower-limit temperature. Considering the reinforcement application, the operating range of the base is roughly above 0 °C. At temperatures below 0 °C, the material is brittle and not resistant towards impact load, whereas at temperatures above T_δ it becomes gradually too soft due to increased viscosity. The temperature-dependent length *l* first expands on

approaching T_δ from below and reaches its maximum value at T_{lmax}= 25.8°C, where l_{max} is 0.9 % longer than the initial length l_o at T = –50 °C. This is followed by shrinkage until T_{lmin}= 48.5°C, where the length reaches its minimum value l_{min} that is 2.9 % shorter than the initial length. Upon further heating, the viscosity component causes continuous lengthening until the end of the test. The discussion of the temperature dependencies of E'', E', tan δ and l will be given in the following paragraphs, by comparing properties of the base to those of the nanocomposites with the MoS_2 addition. The values of T_g, E'_{max}, E'_{Tg}, E'_{RT}, E''_{Tg}, E''_{RT}, T_δ, $\delta_{T\delta}$, T_{lmax}, T_{lmin}, $(l_{max}-l_o)/l_o$ and $(l_o-l_{min})/l_o$ are also collected in Table 1.

B. Change of T_g and the Loss Modulus E'' of the Nanocomposite Coatings

The T_g of the nanocomposite coatings was determined from the maximum in the loss modulus *E''*. The temperature-dependent *E''* of all coatings is shown in Fig. 6. The MoS_2 nanotube addition has shifted the glass transition to higher temperatures. Nanotubes act as stiff cross-points, which impede segmental oscillations of the polymer matrix, so that more thermal energy is needed to excite relaxational motions. In Fig. 6 we observe that the maximum in E'' and the associated T_g of the nanocomposite coatings have shifted from the base value of 18.4 °C into the range 26 – 30 °C (Table 1).

The increased T_g values are randomly scattered within the above temperature range, so that no direct correlation to the concentration of MoS_2 nanotubes can be claimed. The average glass temperature of the nanocomposites is $\overline{T_g}$ = 28.4 ± 1.8 °C for the employed MoS_2 concentration range between 1 % and 15 %, which is by about 10 °C higher than the base value. The loss modulus values E''_{Tg} and E''_{RT} of all coatings are given in Table 1. The differences in the loss modulus maximum value E''_{Tg} between the nanocomposite coatings and the base and between the nanocomposite coatings themselves are only marginal.

C. The Storage Modulus E' of the Nanocomposite Coatings

The temperature-dependent storage modulus *E'* of all coatings is shown in Fig. 7. Within the temperature range suitable for mechanical loading (roughly above 0 °C and before the material gets too soft), the MoS_2 addition has resulted in higher modulus at a given temperature for all concentrations of the nanotubes, i.e., the nanocomposites are generally stiffer. At RT, the E'_{RT} value of the nanocomposites has increased from the base value E'_{RT}= 0.53 GPa into the range 0.93 – 1.18 GPa (Table 1), thus by factors 1.8 – 2.2, so that the storage modulus has practically doubled by the MoS_2 addition. The base + 15 % coating is the stiffest (E'_{RT}= 1.18 GPa), as can be expected for the highest addition of the MoS_2 nanotubes.

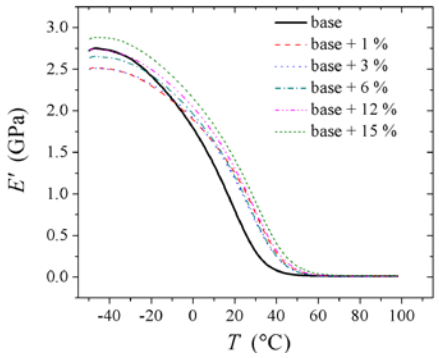

Fig. 7 (Color online) Temperature-dependent storage modulus E' of the investigated coatings. The samples are denoted as the base + vol. % of the MoS_2 nanotubes addition.

The storage modulus values at the glass temperature, E'_{Tg}, of the nanocomposite coatings with different MoS_2 concentrations show only marginal differences, being in the range 0.80 – 0.91 GPa (Table 1). The base value (0.88 GPa) also falls in this range. This demonstrates that, within the temperature range suitable for mechanical loading, the temperature-dependent E' curves of the nanocomposites are roughly translated on the temperature scale by about 10 °C to higher temperatures with respect to the base curve, which is by the amount of the T_g shift due to the nanotubes addition.

The maximum value of the storage modulus, E'_{max}, at T = –50°C deeply in the glass phase shows the following interesting variation with the MoS_2 concentration (Table 1). Firstly, the stiffness of the nanocomposites monotonously increases with the nanotubes concentration. However, the 1, 3 and 6 % nanotubes addition slightly decreases the modulus E'_{max}, below the base value of 2.75 GPa. For the 12 % addition E'_{max} becomes equal to the base value, whereas it becomes larger (2.88 GPa) only for the highest concentration of 15 %. Therefore, adding MoS_2 nanotubes in lower concentrations even decreases the nanocomposite stiffness below the base value deeply in the glass phase and the reinforcement effect in the entire investigated temperature range from –50 °C to 100 °C is only present for high enough

		storage modulus E'			loss modulus E''		tan δ		length			
sample	T_g (°C)	E'_{max} (GPa)	E'_{Tg} (GPa)	E'_{RT} (GPa)	E''_{Tg} (GPa)	E''_{RT} (GPa)	T_δ (°C)	$\delta_{T\delta}$ (°)	T_{lmax} (°C)	T_{lmin} (°C)	$(l_{max}-l_o)/l_o$ (%)	$(l_o-l_{min})/l_o$ (%)
base	18.4	2.75	0.88	0.53	0.23	0.21	42.9	39.0	25.8	48.5	0.9	2.9
base + 1 %	30.3	2.51	0.80	1.04	0.20	0.19	53.6	39.6	36.7	62.4	0.8	2.0
base + 3 %	26.8	2.51	0.86	0.93	0.21	0.22	55.0	45.6	35.0	63.9	0.9	3.8
base + 6 %	27.0	2.65	0.83	0.96	0.22	0.22	54.0	41.7	37.2	62.0	1.1	2.4
base + 12 %	28.5	2.74	0.86	1.05	0.22	0.22	55.8	40.0	38.1	65.1	0.9	2.1
base + 15 %	29.9	2.88	0.91	1.18	0.23	0.22	55.7	36.1	38.1	62.6	0.8	1.5

Table 1 The glass transition temperature T_g, the storage modulus E' (the maximum value E'_{max} at T = –50°C, the value at T_g, E'_{Tg},and the RT value E'_{RT} at T = 25°C), the loss modulus E'' (E''_{Tg} and E''_{RT}), the tan δ parameters (the temperature T_δ of the tan δ peak and the maximum phase lag $\delta_{T\delta}$), and the length parameters (the maximum relative elongation $(l_{max}-l_o)/l_o$ and contraction $(l_o-l_{min})/l_o$, where l_o is the initial length at T = –50°C, and the temperatures T_{lmax} and T_{lmin} of the maximum elongation/contraction).

nanotube concentration (above 12 %). At RT (and generally in the range suitable for mechanical loading), on the other hand, the addition of MoS_2 nanotubes in any concentration reinforces the composite coating, i.e., all nanocomposites are stiffer than the base.

D. The tan δ of the Nanocomposite Coatings

The temperature-dependent tan δ curves of the base and the nanocomposite coatings are shown in Fig. 8. Tan δ is an indicator of how efficiently the material can loose the energy due to molecular rearrangement and internal friction. At the tan δ peak temperature T_δ, molecular bonds are breaking; enabling intense segmental oscillations within the polymer matrix and making the material loosen. The tan δ peaks (and the associated T_δ) of the nanocomposite coatings are shifted to higher temperatures from the base value of T_δ= 42.9°C into the range 53 – 56 °C (Table 1). There is again no pronounced correlation between the T_δ shift and the MoS_2 concentration, so that an average $\overline{T_\delta}$ = 54.8 ± 1.2 °C of the nanocomposites can be defined. The shift of the T_δ temperature by $\Delta T_\delta \approx$ 11°C upon the nanotubes addition is about the same as the shift of the glass temperature ΔT_g and correlates well to the segmental motion obstruction by the nanotubes. Due to the T_δ shift by about 11 °C, the temperature range suitable for mechanical loading of the nanocomposites has also extended to higher temperatures by the same amount. The maximum phase lag $\delta_{T\delta}$ of the nanocomposites obtained from the tan δ peak value falls into the range 36 – 46° (Table 1) with no direct correlation to the MoS_2 concentration. Since the base value (39°) also falls in this range, the nanotubes addition did not change the phase lag significantly.

E. The Length of the Nanocomposite Coatings

The temperature-dependent length of the base and the nanocomposite coatings is shown in Fig. 9. The lengths of all coatings are changing in a similar manner. In the low-temperature part of the experiment between –50°C and about 30°C, the samples are slightly stretching upon heating and the maximum length l_{max} is observed in the glass transition area at a temperature T_{lmax} somewhere between the peaks in E'' and tan δ. The stretching is caused by braking of the intermolecular bonds, the free volume increase and consequent loosening of the structure. After the structural relaxation in the glass transition area takes place, intermolecular forces are established again, the free volume is reduced and the material experiences slight contraction. The entropy is the highest in the most contracted state where the length reaches its minimum value l_{min} at the temperature T_{lmin} slightly higher than T_δ. At still higher temperatures, the viscous component causes further expansion of the material.

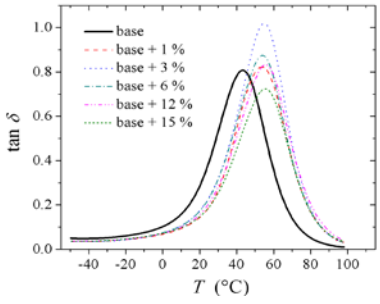

Fig. 8 (Color online) Temperature-dependent tan δ curves of the investigated coatings. The samples are denoted as the base + vol. % of the MoS_2 nanotubes addition.

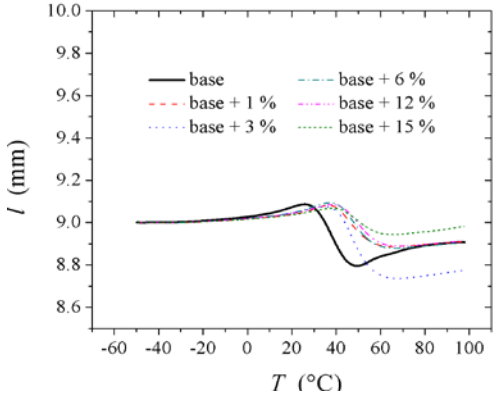

Fig. 9 (Color online) Temperature-dependent length *l* of the investigated coatings. The samples are denoted as the base + vol. % of the MoS_2 nanotubes addition.

Upon adding MoS_2 nanotubes to the polymer matrix, T_{lmax} of the nanocomposites has shifted upwards from the base value of 25.8 °C into the range 35 – 38 °C (Table 1) and the maximum relative elongation $(l_{max}-l_o)/l_o$ with respect to the initial length l_o is in the range 0.8 – 1.1 % (Table 1). The base value (0.9 %) also falls into this range. After the material contraction in the glass transition area, the T_{lmin} values of the nanocomposites have shifted from the base value of 48.5 °C into the range 62°C– 65°C, and the maximum relative contraction $(l_o-l_{min})/l_o$ is in the range 1.5 – 3.8 % (Table 1), where the base value (2.9 %) also falls in this range. Nanotubes addition to the polymer matrix thus shifts the characteristic temperatures T_{lmax} and T_{lmin} to higher temperatures, whereas the maximum relative elongation and contraction are not affected significantly. There is again no noticeable correlation of T_{lmin}, T_{lmax}, l_{min} and l_{max} to the MoS_2 nanotubes concentration.

V. DISCUSSION AND CONCLUSIONS

DMA analysis of the nanocomposite coatings has shown the following changes of their viscoelastic properties with respect to the base coating. The MoS_2 nanotubes addition into the polymer matrix has shifted the glass transition temperature by $\Delta T_g \approx$ 10°C towards higher temperatures. The tan δ peak temperatureT_δ, the temperature range suitable for mechanical loading, the temperatures T_{lmax} and T_{lmin} of the maximum elongation/contraction have shifted towards higher temperatures by about the same amount. These changes originate from the nanotubes incorporation into the polymer matrix, acting as stiff cross-points that impede segmental oscillations, so that more thermal energy is needed to excite internal motions in the nanocomposites. The main benefit of the MoS_2 nanotubes addition is a significant increase of the storage modulus E' within the temperature range suitable for mechanical loading, being at RT roughly a factor of 2 larger than E' of the base. The stiffness of the nanocomposites has thus increased quite significantly by the nanotubes addition. The coating with the highest MoS_2 concentration of 15 % is the stiffest, with its E'_{RT} value being a factor 2.2 larger than that of the base. At low temperatures deeply in the glass phase of the polymer matrix, the reinforcement effect depends on the MoS_2 concentration. Slight reinforcement (an increase of the storage modulus E'_{max} by about 5 % from the base value) is observed only for the highest concentration of 15 %, whereas at lower concentrations, E'_{max} of the nanocomposites

is equal or even smaller than the storage modulus of the base. Therefore, adding MoS_2 nanotubes in lower concentrations decreases the nanocomposite stiffness below the base value deeply in the glass phase and the reinforcement effect in the entire investigated temperature range from –50 °C to 100 °C is only present for high enough nanotubes concentration (above 12 %). At RT (and generally in the range suitable for mechanical loading), on the other hand, the addition of MoS_2 nanotubes in any concentration reinforces the composite coating, i.e., all nanocomposites are stiffer than the base.

Comparing the reinforcement performance of our MoS_2–containing nanocomposite to some other known nanocomposites, we note that the nanocomposite of a nylon 6 matrix with montmorillonite (MMT) clay nanofillers shows similar degree of reinforcement [15]. The storage modulus of the nylon 6 matrix (E= 2.75 GPa) is the same as that of our base coating, whereas the storage modulus of the MMT nanofiller (178 GPa) is also comparable to that of the MoS_2 nanotubes [5]. The modulus increase of the nylon 6 nanocomposite containing 3 vol. % of the MMT nanofiller was reported to be by a factor 2.1, which is about the same as for our MoS_2–based nanocomposite. For the multi-walled carbon nanotubes mixed in different concentrations into different polymers (PMMA, PS, PC, PA6, nylon), the modulus increase was reported to be by factors between 1.1 and 3.1 (see Table 2 of ref. [2] and references therein), whereas for the single-walled carbon nanotubes the modulus increase was by factors between 1.6 and 3.5 (see Table 3 of ref. [2] and references therein). The reinforcement performance of our MoS_2-based nanocomposites with the modulus increase by a factor about 2 thus compares well to that of the carbon nanotubes– and the MMT–reinforced nanocomposites.

ACKNOWLEDGEMENT

We thank Dr. Kristina Žagar from J. Stefan Institute for her help in TEM experiments.

REFERENCES

[1] See, for a review: D.R. Paul and L.M. Robeson, Polymer 49 (2008) 3187-3204, and references therein.

[2] See, for a review: J.N. Coleman, U. Khan, W.J. Blau and Y.K. Gun'ko, Carbon 44 (2006) 1624-52, and references therein.

[3] R. Tenne, Colloids and Surfaces A: Physicochem. Eng. Aspects 208 (2002) 83-92.

[4] M. Remškar and A. Mrzel, Vacuum 71 (2003) 177-83.

[5] Kis, D. Mihailovic, M. Remskar, A. Mrzel, A. Jesih, I. Piwonski, A.J. Kulik, W. Benoît and L. Forró, Adv. Mater. 15 (2003) 733-6.

[6] L. Joly-Pottuz, F. Dassenov, M. Belin, B. Vacher, J.N. Martin and N. Fleischer, Tribol. Lett. 18 (2005) 477-85.

[7] L. Rapoport, N. Fleischer and R. Tenne, J. Mater. Chem. 15 (2005) 1782-8.

[8] M. Chhowalla and G.A. Amaratunga, Nature 407 (2000) 164-7.

[9] Y.Q. Zhu, T. Sekine, Y.H. Li, W.X. Wang, M.W. Fay, H. Edwards, P.D. Brown, N. Fleischer and R. Tenne, Adv. Mater. 17 (2005) 1500-3.

[10] J. Chen, S.L. Li and Z.L. Tao, J. Alloys Compd. 356-357 (2003) 413-7.

[11] Zak, Y. Feldman, V. Lyakhovitskaya, G. Leitus, R. Popovitz-Biro, E. Wachtel, H. Cohen, S. Reich and R. Tenne, J. Am. Chem. Soc. 124 (2002) 4747-58.

[12] J. Chen, Z.L. Tao and S.L. Li, Angew. Chem. Int. Ed. 42 (2003) 2147-51.

[13] M. Remškar, A. Mrzel, M. Viršek and A. Jesih, Adv. Mater. 19 (2007) 4276-8.

[14] M. Remškar, M. Viršek and A. Mrzel, Appl. Phys. Lett. 95 (2009) 133122.

[15] T.D. Fornes and D.R. Paul, Polymer 44 (2003) 4993-5013